Palaeogeography, Palaeoclimatology, Palaeoecology 543 (2020) 109582

Contents lists available at ScienceDirect

Palaeogeography, Palaeoclimatology, Palaeoecology

journal homepage: www.elsevier.com/locate/palaeo

Seawater paleotemperature and paleosalinity evolution in neritic environments of the Mediterranean margin: Insights from isotope analysis of bivalve shells

J. Briard[a,b,*], E. Pucéat[b], E. Vennin[b], M. Daëron[c], V. Chavagnac[a], R. Jaillet[b], D. Merle[d], M. de Rafélis[a]

[a] Géosciences Environnement Toulouse (GET), Université Paul Sabatier Toulouse 3, CNRS UMR 5563, IRD, 14 avenue Edouard Belin, F-31400 Toulouse, France
[b] Biogéosciences, UMR 6282, UBFC/CNRS, Université Bourgogne Franche-Comté, 6 boulevard Gabriel, F-21000 Dijon, France
[c] Laboratoire des Sciences du Climat et de l'Environnement, LSCE/IPSL, CEA-CNRS UVSQ, Université Paris-Saclay, F-91191 Gif-sur-Yvette, France
[d] Muséum National d'Histoire Naturelle, UMR CRNS 7207 (CR2P-MNHN, CNRS, UPMC-Paris 6), Sorbonne Universités, 8 rue Buffon, F-75005 Paris, France

ARTICLE INFO

Keywords:
Paleoclimate
Middle Miocene Climatic Optimum
Clumped isotopes
Hydrological cycle
Coastal environment

ABSTRACT

The first step of ice-sheet build-up on Antarctica at the Eocene-Oligocene boundary was followed by a phase of climate instability culminating during the Miocene with a warming event called the Middle Miocene Climate Optimum (MMCO), that ended with a marked cooling phase identified as the Middle Miocene Climate Transition (MMCT). While numerous benthic foraminifera $\delta^{18}O$ and Mg/Ca data have been used to capture the global climate evolution during this interval of climate and ice-sheet instability, geochemical records from shallow-water carbonates still remain scarce. Yet such records are crucial to capture the diversity of regional environmental responses to global climate changes, and thus to better understand the behavior of our climate system during this critical interval. In this work, we test the potential of a multi-proxy approach ($\delta^{18}O$, clumped isotope (Δ_{47}), strontium isotopes ($^{87}Sr/^{86}Sr$)) applied to bivalves recovered from the Liguro-Provencal Basin and Rhodano-Provencal basin (Northwestern of the Mediterranean Sea) to reconstruct the evolution of shallow seawater temperature and salinity in this region over the latest Oligocene to Middle Miocene interval (~10 Myrs). Our results highlight a local cooling in the northwestern Mediterranean Sea during the MMCO that contrasts with the warming observed in other regions, with seawater temperatures inferred from Δ_{47} analyses in the 13–18 °C range. These cool seawater temperatures recorded in the studied region during the MMCO are much cooler than those recorded in the open oceans, but are in agreement with the proliferation of bryozoan observed in the Castillon-Du-Gard area during this interval. Low bivalve $\delta^{18}O$ values (−3.24‰ in average) are recorded during this episode are interpreted to reflect enhanced freshwater inputs, lowering local salinity and seawater $\delta^{18}O$. Such enhanced freshwater inputs point to a phase of enhanced hydrological cycle in the studied region, possibly linked to the global mid-Miocene warming event. Bivalve $^{87}Sr/^{86}Sr$ data mostly fall within the global seawater Sr isotope reference curve, but remain compatible with enhanced freshwater inputs during the Aquitanian and during the Langhian, as these inputs were probably not important enough to induce a large departure from the seawater curve at a regional scale.

1. Introduction

A major feature of the long-term climate evolution during the Cenozoic is the transition from the "greenhouse" conditions of the late Early Eocene (~50 million years ago) to the modern "icehouse" climate mode with its much lower atmospheric CO_2 levels and permanent polar ice-sheets on both poles (Zachos et al., 2008). This transition occurred through a series of steps, beginning with the abrupt global cooling recorded at the Eocene/Oligocene transition (Zachos et al., 1996; Lear et al., 2008; Liu et al., 2009; Galeotti et al., 2016; Cramwinckel et al., 2018) followed by a period of instability of the Antarctic ice-sheet during the Oligocene and part of the Miocene (Billups and Schrag, 2002; Lear et al., 2015; Gasson et al., 2016). This period of instability is marked by several warming and cooling phases associated with waxing

* Corresponding author at: Géosciences Environment Toulouse (GET), Université Paul Sabatier Toulouse 3, CNRS UMR 5563, IRD, 14 avenue Edouard Belin, F-31400 Toulouse, France.
E-mail address: justine.briard@get.omp.eu (J. Briard).

https://doi.org/10.1016/j.palaeo.2019.109582
Received 6 September 2019; Received in revised form 19 December 2019; Accepted 26 December 2019
Available online 09 January 2020

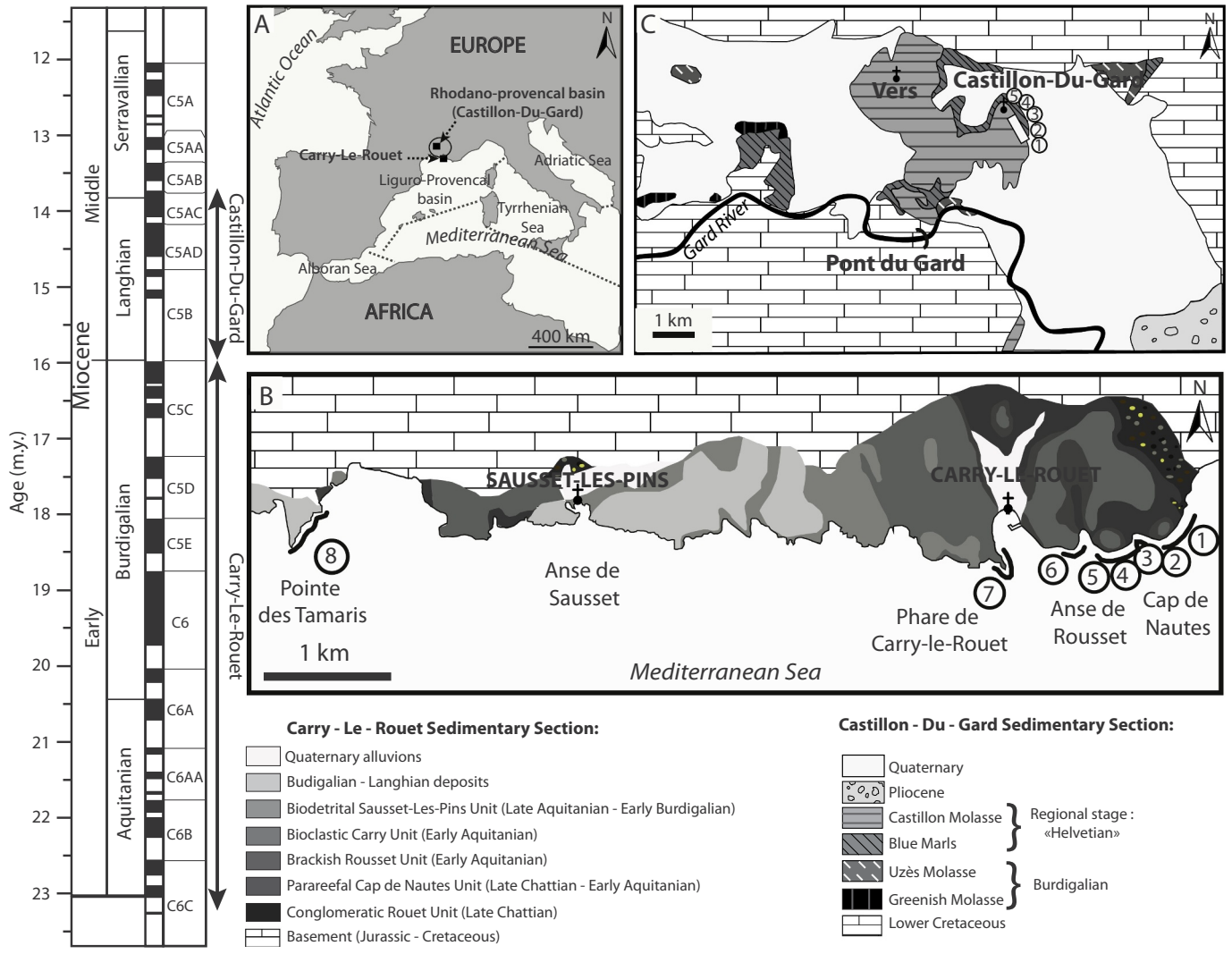

Fig. 1. Location of the studied outcrops. Absolute ages presented on the left are from Ogg et al. (2016), along with the correspondence with magnetostratigraphic frame and foraminifera zonation (C6C to C5A). A. Location of the outcrops on a modern map of the North Western Mediterranean area. B. Geological map of outcropping latest Chattian to latest Burdigalian (Oligo-Miocene) formations in the Coastal Nerthe area and their sedimentary units (modified from Andreieff et al., 1972; Oudet et al., 2010; Demory et al., 2011). The numbers 1 to 8 correspond to logs positions used to build a composite log of over than 80 m, that is used in this study. C. Geological map of Burdigalian to earliest Serravallian (Miocene) formations in the Castillon-Du-Gard sub-basin and their sedimentary units (modified by from Reynaud et al., 2012). The numbers 1 to 5 correspond to logs positions.

and waning of the Antarctica ice-sheet. This includes the Late Oligocene Warming Event, the cooling at the Oligocene-Miocene boundary (~23.03 Ma, Mi-1 event), and the global warming event leading to the Middle Miocene Climatic Optimum (MMCO, ca. 16 Ma to ca. 14.5 Ma) during the latest Early to Middle Miocene interval (e.g. Zachos et al., 2008; Mawbey and Lear, 2013; Beddow et al., 2016; Goldner et al., 2014; Holbourn et al., 2015; Super et al., 2018). This phase of instability ended with the marked cooling of sea surface temperature (SST) defined as the Middle Miocene Climate Transition (MMCT, ca. 14.5 to ca. 13.5 Ma), associated once more with a large-scale expansion of the Antarctic ice-sheet (Holbourn et al., 2005; Foster et al., 2012). Although the first development of permanent ice-sheets on Antarctica during the Eocene-Oligocene cooling event has been extensively studied in the past decades (Zachos et al., 1996; Ivany et al., 2000; Lear et al., 2008; Liu et al., 2009; Tremblin et al., 2016), little is known about the following interval of ice-sheet instability. For the earliest Oligocene to the middle Miocene interval (~ 10 million years), most paleoclimatic records available to date are based on isotopic ($\delta^{18}O$) and elemental (Mg/Ca) composition of benthic foraminifera that record the physico-chemical features of ocean bottom water temperature (Pagani et al., 1999; Miller et al., 1991; Diester-Haass et al., 2009). Marine surface temperature records are scarce, mostly based on various geochemical measurements on planktonic organisms (e.g. $\delta^{18}O$, Mg/Ca, TEX_{86}, $U_{37}^{K'}$), and are restricted to limited time intervals (Pagani et al., 1999; Super et al., 2018). Palynological data or fauna distribution give further information on paleoenvironmental conditions on the continents (Bruch et al., 2004; Jiménez-Moreno and Suc, 2007; Pound et al., 2012). However, archives from coastal environments such as bivalves remain understudied for this time period despite their location in a transitional environment between continent and ocean important to characterize as well to obtain a global view of the response of climate to perturbations. Bivalves recovered from shallow-water environments (< 50 m, Stenzel, 1971) have been successfully used to document temperature and/or salinity variations in the past (Klein et al., 1996; Kirby et al., 1998; Steuber et al., 2005; Schöne and Giere, 2005; Huyghe et al., 2012, 2015; Bougeois et al., 2014, 2016; Mouchi et al., 2018; de Winter et al., 2018). Bivalves like oyster shells offer key advantages for paleotemperature reconstructions in coastal area, as (1) they are formed of low-magnesian calcite, thus quite resistant to recrystallization (Brand and Veizer, 1981; Al-Aasm and Veizer, 1986; Ulmann and

Korte, 2015), (2) they have a large spatial and temporal distribution and (3) they live fixed on a substratum during several years, allowing reconstruction of local seasonal variations of environmental parameters (temperature and salinity), which cannot be assessed with foraminifera. In coastal environments, reconstruction of shallow water temperatures using bivalve $\delta^{18}O$ can however be impeded by local seawater $\delta^{18}O$ ($\delta^{18}O_{sw}$) variability due to local processes such as evaporation, precipitation, surface runoff and groundwater discharges. One way to overcome this limitation is to combine conventional oxygen isotope ($\delta^{18}O$) with clumped isotope (Δ_{47}) analyses of bivalves because carbonate clumped isotope (Δ_{47}) composition is solely linked to temperature during mineral formation, and independent from the isotopic composition of the ambient water (Ghosh et al., 2006; Schauble et al., 2006; Eiler et al., 2009; Henkes et al., 2013). Additional information on environmental conditions is provided by the Sr isotopic system applied on bivalves, as the $^{87}Sr/^{86}Sr$ ratios recorded in their umbo has been shown to record the occurrence of large freshwater discharge in their living marine environment (Ingram and Sloan, 1992; Bryant et al., 1995; Widerlund and Andersson, 2006; El Meknassi et al., 2018; Zaky et al., 2018).

In this context, we propose to test the potential of a multi-proxy approach applied on bivalves thriving in coastal environments to reconstruct the evolution of shallow (< 50 m) seawater temperatures over the latest Oligocene to Middle Miocene interval. The two selected outcrops, i.e. Carry-Le-Rouet and Castillon-Du-Gard located within the Liguro-Provencal and Rhodano-Provencal Basins (SE of the Mediterranean Sea, France), present sediments deposited in shallow (< 50 m) open marine conditions with abundant bivalve shells. In both localities, a well-constrained chronostratigraphic framework is available (Andreieff et al., 1972; Oudet et al., 2010; Ferrandini et al., 2010; Demory et al., 2011). Our new dataset provides new information on temperature, salinity and runoff evolution within a still understudied region. The outcomes contribute to better constrain the regional environmental response to global climatic changes during this key interval of Antarctica ice-sheet waning and waxing.

2. Geological setting

The modern western Mediterranean Sea is structured into four basins (Fig. 1A): Alboran Sea, Adriatic Sea, Tyrrhenian Sea, and Liguro-Provencal basin that extends from the Gulf of Genoa in the East to the Strait of Gibraltar in the West to Sardinia in the South. These basins began to form by the end of the Oligocene (~23.03 Ma) and reached their full extension during the Miocene (23.03–5.33 Ma) (Rehault et al., 1984). The oceanization of the Liguro-Provencal basin corresponds to the opening of a back-arc basin associated with the eastward retreat of an Adriatic/ionian slab sinking into the mantle (Gueguen et al., 1998; Faccenna et al., 1997; Gattacceca et al., 2007; van Hinsbergen et al., 2019). During the Miocene marine transgression, a second basin started to form in the Rhône Valley, called the Rhodano-Provencal Basin. This basin is located north of the Liguro-Provencal Basin, at the junction between the perialpine foreland basin to the north and the northern margin of the western Mediterranean to the south. The Rhodano-Provencal Basin extends to the north as a channel that follows the alpine chain from Marseille (France) to Vienna (Austria). The pre-Miocene structuration of the Rhodano-Provencal Basin results in a highly differentiated topography organized in sub-basins (e.g. Valreas, Sommières, Uzès and Castillon-Du-Gard). Due to this inheritance, the Rhodano-Provencal sub-basins evolved independently of each other during the Miocene marine transgression. The two outcrops selected for this study are located within the Liguro-Provencal (Carry-Le-Rouet) and Rhodano-Provencal (Castillon-Du-Gard) basins (Fig. 1A).

2.1. Carry-Le-Rouet outcrops in the Coastal Nerthe area

On the northern part of the Liguro-Provençal Basin (Fig. 1B), a ~100 m succession of Late Oligocene (Chattian) to Early Miocene (Burdigalian) continental and marine sediments crops out along the Blue coast (43°19′50.19″N, 5°09′05.67″E), at Carry-Le-Rouet (20 km west of Marseille, France). The sedimentary succession is separated by a major unconformity from the deformed and eroded Mesozoic basement called Nerthe Massif. The Barrémo-Aptian basement (Urgonian facies) is a thrust structure resulting from the Eocene Pyrenean compression (Tempier, 1987). The outcrops are exposed along the coast on 8 km and the sediments are organized in six lithostratigraphic units extending from the Cap de Nautes to the Pointe de Tamaris (Fig. 1B; Andreieff et al., 1972; Maurel-Ferrandini, 1976). The basal Conglomeratic Rouet unit (Unit 1, Chattian) is characterized by a transition from fluvial to deltaic depositional environments. The following formations (Para-reefal Cap de Nautes unit (Unit 2), the Brackish Rousset unit (Unit 3), the Bioclastic Carry unit (Unit 4), the Biodetrital Sausset unit (Unit 5) and the Plan de Sausset unit (Unit 6)) correspond to an alternation of marine to continental-marine transitional depositional environments. This succession benefits from a well-constrained biostratigraphic record using calcareous nannofossils and planktonic foraminifera (Oudet et al., 2010), supplemented with magnetostratigraphy (Demory et al., 2011). Despite the presence of hiatus along the Chattian to Burdigalian succession, the interval sampled in this study did not record any major stratigraphic gaps considering the sedimentary succession continuity and the age model proposed by Demory et al., 2011.

2.2. Castillon-Du-Gard outcrops

The Castillon-Du-Gard Sub-basin (43°58′12.61″N, 4°33′16.05″E) of the Rhodano-Provencal Basin (Fig. 1C) presents marine deposits of lower to middle Miocene in age (Demarcq, 1970). This Sub-basin rests above a thick Mesozoic succession in a corridor and is separated from the main Rhodanian basin by the N040° Nîmes Fault (Reynaud et al., 2012). The sediments are organized into five lithostratigraphic formations (Greenish Molasse, Saint-Siffret Marls, Uzès Molasse, Blue Marls and Castillon Molasse, respectively) ranging from the Burdigalian to the regional “Helvetian” stage (Langhian-Serravallian equivalent; Fig. 1C). Only “Helvetian” stage is presented here, which is in temporal continuity with the Carry-Le-Rouet outcrops. The Helvetian stage at Castillon-Du-Gard Sub-basin is organized into two distinct formations (Fm.): the blue marls at the base and the Castillon Molasse at the top. The blue marls Fm. varies laterally in thickness from a few meters to 70 m-thick. They consist mainly of lithoclasts composed of calcite, feldspar, glauconite, muscovite and iron oxide grain and planktonic and benthic foraminifera, echinoderms, bryozoans and mollusks (Reynaud et al., 2012). The Castillon Molasse is about 70 m-thick and is composed of a bryozoan and mollusk packstone-rudstone (Bryomol; Reynaud et al., 2012). It is subdivided into two sub-formations: the Vers Unit at the base and the Castillon Unit s.s at the top. The presence of glauconite and oxide of iron in the Vers unit gives a characteristic yellow colour to the Bryomol packstone rich in pectenids encrusted by oysters, barnacles and bryozoans. Castillon Unit s.s is a Bryomol floatstone differs from the Vers Unit by the occurrence of green and red algae (Reynaud et al., 2012).

The depositional setting corresponds to an offshore environment for the Blue Marls, protected from currents and waves. The Castillon Molasse is interpreted as being deposited in a shallow tidal bay (Reynaud et al., 2012). The stability and homogeneity of the florofaunal assemblages throughout the whole sedimentary succession are indicative of open marine conditions without major variation in salinity Reynaud et al., 2012).

Several hundred oyster shells were collected on about thirty different levels of the Carry-Le-Rouet section. All these oysters belong to the *Ostrea* genus and some have been determined to be *Ostrea fimbriata* species. A hundred oyster shell fragments were collected on about twenty different levels for the Castillon-Du-Gard section, unfortunately the sample size did not allow the species identification.

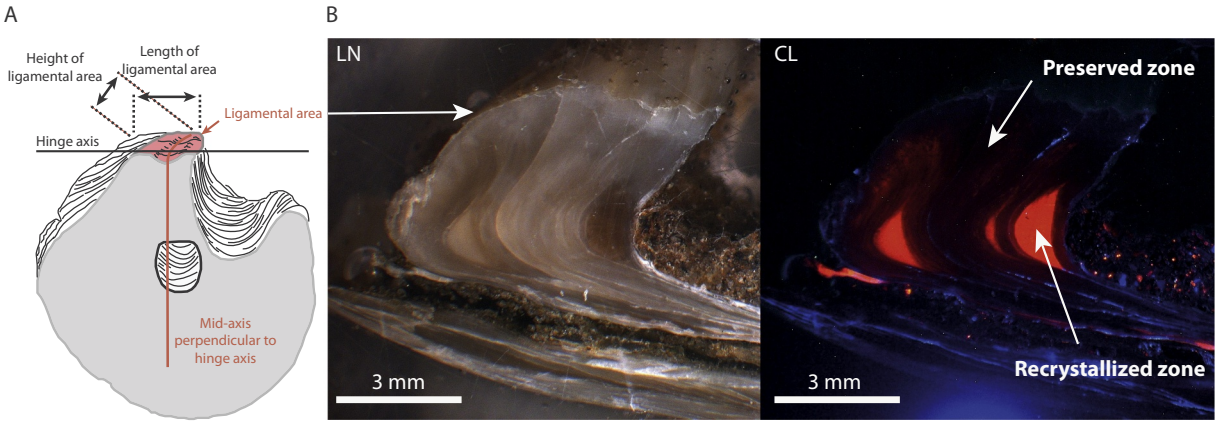

Fig. 2. A. Picture representing the location of ligamental area on an oyster shell (modified from Stenzel, 1971). B. Sections of oyster shells under natural light (LN) and cathodoluminescence (CL), showing luminescent part in orange (mainly chalky areas) and non-luminescent to weakly luminescent parts with identifiable seasonal patterns of growths. Only the non-luminescent to weakly luminescent parts with identifiable seasonal patterns of growths parts have been sampled for isotopic analyses.

3. Materials and methods

3.1. Preservation of the studied material

Each oyster shell was embedded in Araldite ® 2020 resin from Huntsman (Basel, Switzerland), sawed perpendicularly to growth lines along the major growth axis (Fig. 2A), and carefully polished. Polished sections were observed under cathodoluminescence microscopy (CL) to assess the preservation state of each shell. CL analyses were carried out on a luminoscope (ELM – 3R) coupled to LEICA MZ12 microscope surmounted by a camera Lumenera Infinity 3. Luminescent areas with large unorganized calcite crystals (mainly chalky areas that are more sensitive to recrystallization; Kirby et al., 1998; Lartaud et al., 2006; Ullmann et al., 2013; de Winter et al., 2018) and non-luminescent to weakly luminescent areas with identifiable seasonal patterns of growths (Fig. 2B) of each shell section were precisely mapped. The luminescent areas are representative of recrystallized calcite and have not been sampled for isotopic analyses. Only the non-luminescent to weakly luminescent parts of the shells, where a slight luminescence follows the seasonal patterns of growths (induced by natural incorporation of Mn^{2+} in calcitic structure; Langlet et al., 2006), have been sampled for $\delta^{18}O$, Δ_{47} and $^{87}Sr/^{86}Sr$ analyses, according to recent works (Lartaud et al., 2010; Huyghe et al., 2015; Bougeois et al., 2016). The Carry-le-Rouet and Castillon-Du-Gard outcrops only encountered a shallow burial (< 100 m; Reynaud et al., 2006; Hamon et al., 2013; Seibel and James, 2017) as evidenced by the absence of compaction traces and the absence of younger sediment deposition in the region. Such shallow burial depths (Choquette and James, 1990) ensures that the sediments have not encountered large overburden pressure or elevated temperatures. This argues for an absence of solid-sate reordering in the analyzed bivalve shells and therefore a preservation of initial Δ_{47} signal.

3.2. Oxygen isotope analyses

For this study, 534 samples were recovered from 101 shells. For most of the shell fragments, 1 to 3 different powder sample have been collected, each of them by gathering carbonate powder along a transect perpendicular to the growth line of the individual shell, in order to average the $\delta^{18}O$ value over at least part of the oyster life and minimize the variability within and between shells from a single stratigraphic level. For 6 of the largest oyster shells, a microsampling along a transect perpendicular to the growth lines was performed in the ligamental area (Fig. 2A) to assess the variability of isotopic signal during at least part of the bivalve life. For these shells, the $\delta^{18}O$ value of each measurement along this transect is reported on Suppl. Table 1 in bold. The recovered powders were analyzed for its oxygen isotope composition: 30 to 40 µg of calcite collected using a scalpel reacted with 100% phosphoric acid at 70 °C using a KIEL IV Carbonate Device connected to a Delta V Plus Isotope ratio mass spectrometer at the Biogeosciences Laboratory (University of Burgundy, Dijon, France). Oxygen isotope compositions have been corrected from the instrumental drift and are reported in the standard delta notation relative to VPDB (Vienna PeeDee Belemnite) in ‰ by assigning a $\delta^{18}O$ value of - 2.20‰ to NBS19. External reproducibility was better that ± 0.08‰ (1 σ_E) for oxygen isotopes based that on multiple analyses of NBS19 along the runs. Carbon isotopes (Suppl. Table 1) measured at the same time are also reported in the delta notation relative to VPDB in ‰ by assigning a $\delta^{13}C$ value of +1.95‰ to NBS19. Carbon isotope reproducibility is better than ± 0.04‰ (1 σ_E).

3.3. Clumped-isotope analyses

Carbonate clumped-isotope thermometry is based on the quantification of statistical anomalies in the abundance of doubly substituted isotopologues of carbonate groups (e.g., $^{13}C^{18}O^{16}O^{16}O^{2-}$). For thermodynamic reasons, the equilibrium abundance of $^{13}C–^{18}O$ bonds in a carbonate mineral increases as temperature decreases (e.g. Schauble et al., 2006), and this isotopic signal may be preserved over geological time scales under favourable conditions (Passey and Henkes, 2012; Stolper and Eiler, 2015). By precisely measuring the abundance of the multiply-substituted, mass-47, isotopologues in the CO_2 produced by acid digestion of a carbonate sample it is thus possible to constrain its original crystallization temperature without making assumptions regarding the composition of parent waters (Ghosh et al., 2006; Eiler et al., 2009).

Δ_{47} analyses generally require larger amounts of material than conventional, “single-isotope” analyses, and their precision and accuracy are ultimately limited by ion counting statistics and standardization issues. Each analysis reported here required from 2 to 3.5 mg, and two or three replicate analyses per sample were performed (Table 2).

At Carry-Le-Rouet, nine of the larger shells already analyzed for $\delta^{18}O$ were selected for Δ_{47} measurements. For the largest oyster (CAR17-6-33-b), two sub-sample carbonate powders were collected separately from sections of the shell corresponding to minimum and maximum $\delta^{18}O$ values, respectively. For the remaining shells, carbonate powder was collected from the entire preserved oyster section (foliated calcite). At Castillon-Du-Gard, due to the small size of the available bivalve fragments, each sample comprised carbonate from several shell fragments collected from the same stratigraphic level or from adjacent stratigraphic levels. Overall, samples were collected from 3 different stratigraphic levels, corresponding to levels 9–12 m,

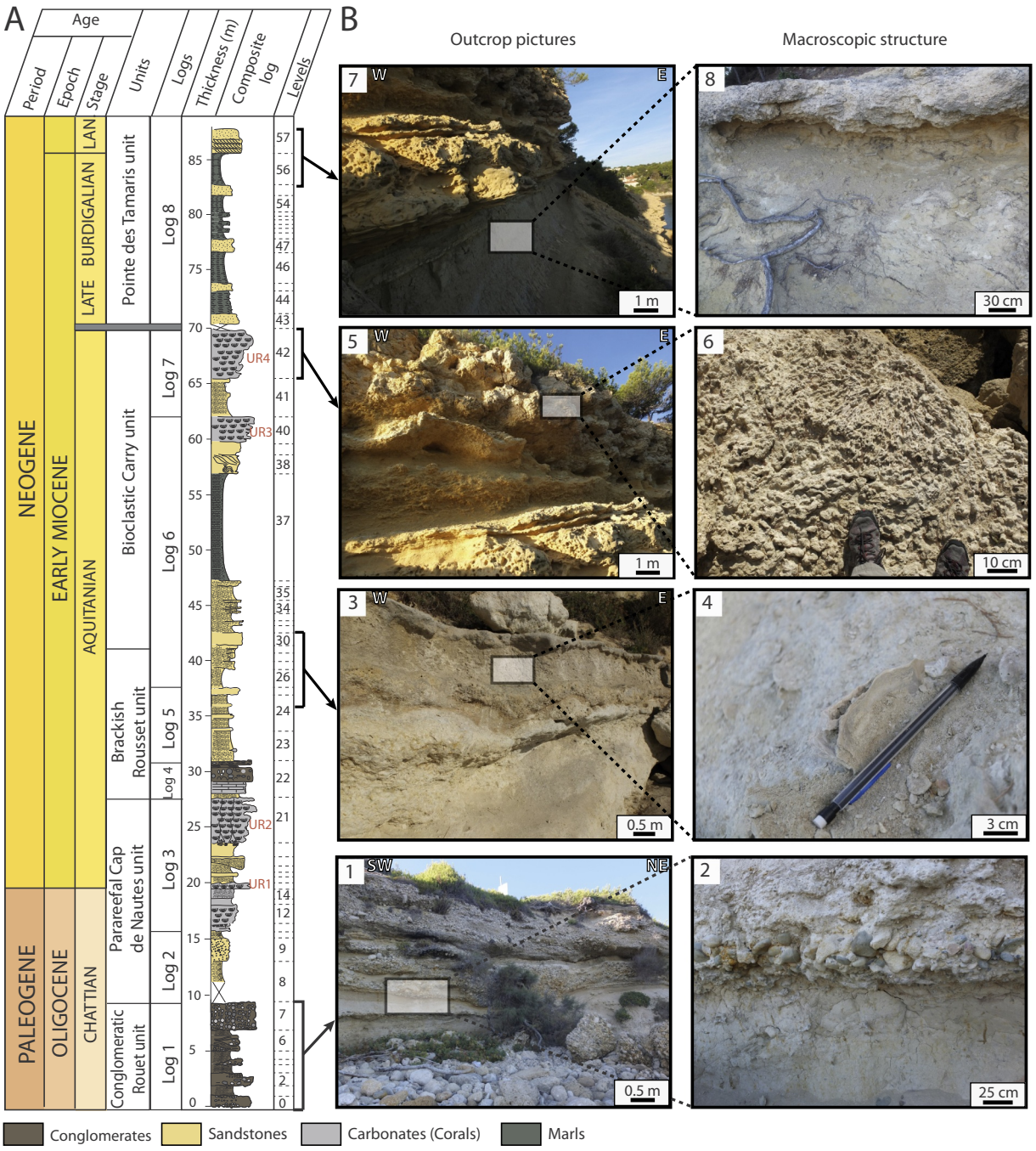

Fig. 3. A. Composite log of the Carry-Le-Rouet sedimentary succession with the different units identified along the log (after Andreieff et al., 1972; Oudet et al., 2010; Demory et al., 2011), lithologies and marker beds (UR1 to UR4 in red). The position of logs 1 to 8, used to build this synthetic log, is reported on Fig. 1. B. Outcrop pictures: 1. Transition from continental conglomerate to marine sandstone in the Chattian Conglomeratic Rouet unit; 2. Detail of the conglomerate beds eroding sandstones with oyster debris in the Conglomerate Rouet Unit. 3. Bioclastic carbonate deposits with abundant oyster shells at the transition between the Brackish Rousset and the Bioclastic Carry units; 4. *Ostrea fimbriata* localized at the base of the Bioclastic Carry unit; 5. Reefal Unit 4 (UR4) outcropping the Bioclastic Carry unit in Carry harbor; 6. Detail of the surface topping the UR4 and composed of dense Poritidae corals preserved in life position; 7. Marls of Tamaris section covered by the Langhian carbonate deposits; 8. Detail of marls with a low fossil record. (For interpretation of the references to colour in this figure legend, the reader is referred to the web version of this article.)

13–17 m, and 19.5–20.5 m.

The 13 clumped-isotope samples (considered of 2 or 3 aliquots each) were analyzed at LSCE (Laboratoire des Sciences du Climat et de l'Environnement) using the equipment and procedures described by Peral et al. (2018). Carbonate powders were dissolved in a common, stirred, 104% phosphoric acid bath at 90 °C for 15 min. After cryogenic removal of water, the evolved CO_2 passed through a Porapak Q column (50/80 mesh, 1 m length, 2.1 mm ID) held at −20 °C under helium 6.0 flow (25 mL/min). CO_2 was then quantitatively recollected by cryogenic trapping, and transferred by gas expansion into an Isoprime 100 dual-inlet mass spectrometer equipped with six Faraday collectors (*m/z* 44 to 49). Each analysis took about 3 h, during which sample gas and working reference gas were allowed to flow from matching, 10 mL reservoirs into the source, through a pair of fused silica capillaries (65 cm length, 110 μm ID). Every 20 min, gas pressures were adjusted to achieve a mass 44 current of 40 nA, with differences between sample

and reference gas generally below 0.1 nA. Background currents were measured in all high-gain collectors (m/z 45 to 49) before and after each pressure adjustment, with gas flowing into the source, and are found to strongly correlate with the mass 44 current. Background-corrected ion current values were processed using the IUPAC ^{17}O-correction parameters (Brand et al., 2010) to compute $\delta^{13}C_{VPDB}$, $\delta^{18}O_{VPDB}$ and "raw" Δ_{47} values for each analysis. The isotopic composition ($\delta^{13}C$, $\delta^{18}O$) of our working reference CO_2 was computed based on nominal $\delta^{13}C_{VPDB}$ and $\delta^{18}O_{VPDB}$ values for carbonate standard ETH-3 ($\delta^{13}C_{VPDB}$ = 1.71‰, $\delta^{18}O_{VPDB}$ = −1.78‰, Bernasconi et al., 2018) and an oxygen-18 acid fractionation factor of 1.008176 (Das Sharma et al., 2002). Three carbonate standards, ETH-1 to ETH-3 (Meckler et al., 2014; Bernasconi et al., 2018), were then used to convert raw Δ_{47} to "absolute" Δ_{47} values, following the procedure described by Daëron et al. (2016). The nominal Δ_{47} values for these standards are those recomputed by Bernasconi et al. (2018) using IUPAC parameters: 0.258‰ for ETH-1, 0.256‰ for ETH-2 and 0.691‰ for ETH-3. The overall external reproducibility (standard deviation) of clumped isotopes measurements for bivalve shells and standard is 14.6 ppm (n = 86).

3.4. Strontium isotope analyses

Twelve of the thirteen clumped-isotope samples were also analyzed for $^{87}Sr/^{86}Sr$ ratios. About 10 mg of carbonate powder were dissolved in a savillex beaker with 1 ml solution of 2 N HNO_3 on a hot plate at 70 °C. The Sr was isolated from the matrix using conventional Eichrom Sr-Spec columns. The strontium isotopic composition is measured using a Thermo Triton Plus thermal ionization mass spectrometers at the GET laboratory (Toulouse, France). The $^{87}Sr/^{86}Sr$ ratios were defined as the average of 150 measurements of ion intensities following the static multi-collection mode normalized to $^{86}Sr/^{88}Sr$ = 0.1194. During the measurement period, the standard NBS 987 gave $^{87}Sr/^{86}Sr$ values of 0.710281 ± 0.000008 (2 σ_D, n = 4). The accuracy of our measurements is verified against the measured ratios of international standards: 1) Jct-1 Giant Clam *Tridacna gigas* standard with a measured value of 0.709175 ± 0.000010 (2σ_D; n = 7) and a certified value of 0.709150 ± 0.000050 (Ohno and Hirata, 2007); 2) CAL-S carbonate standard with a measured value of 0.706955 ± 0.000008 (2 σ_D; n = 4) and a certified value of 0.706924 ± 0.000018 (Yeghicheyan et al., 2013); and 3) IAPSO seawater standard with a measured value of 0.709181 ± 0.000003 (2s_D; n = 4) and a certified value of 0.709179 ± 0.000005 (Nayar et al., 2014). All $^{87}Sr/^{86}Sr$ ratios measured on our samples were adjusted to the NBS 987 standard reference value of 0.710250.

4. Results

4.1. Sedimentary study

4.1.1. Carry-Le-Rouet outcrops

In the Carry-Le-Rouet section, the transitional continental to shallow marine depositional environments develops following an E-W polarity. Four facies associations are organized in four main depositional environments: (1) continental to coastal plain; (2) upper shoreface; (3) restricted upper shoreface and (4) lower shoreface (Fig. 3A). Facies descriptions are summarized in Table 1 and environmental interpretations are given below.

4.1.1.1. Continental to coastal plain environment. This environment groups facies A1 to A4 (Table 1). The presence of pedogenetic horizons with rhizoliths, rare plant remains, mottling and carbonate nodules indicate widespread subaerial, episodic sedimentation and soil formation. The marly deposits are crosscut by sandy to conglomerate channels that correspond to sediment discharges in a proximal alluvial plain (Miall, 1986). A1 is interpreted as a flood plain (Nury, 1990; Demory et al., 2011). The clast-supported channels (Table 1; Fig. 3B1 and B2) and lobe-shape conglomerates (A3 and A4) are interpreted as deltaic distributaries (Demory et al., 2011) or alluvial fan delta (Nemec and Steel, 1988). The composition of the conglomerates indicates several sources with a Nerthe (Barremian stage) carbonate origin for the monogenic ones and Paleozoic basement (Permo-Triasic radiolarites or quartzites) for the polygenic conglomerates (Demory et al., 2011). The presence of oysters encrusting the conglomerate boulders is indicative of at least partly marine conditions during the deposition of the distal alluvial fan system (Holmes, 1965), as oysters can be found in brackish or estuarine conditions.

4.1.1.2. Marine environment: coastal plain to outer-platform. This environment encompasses facies B1 to D2 (Table 1). B1 consists of bioturbated sandstones with cordon-rich conglomerates organized in planar stratifications. B1 is interpreted as a coastal shallow marine environment in an upper shoreface (Table 1; Fig. 3B3 and B4; Nemec and Steel, 1988). The fine to coarse sandstones (B2) with megaripples, Hummocky Cross-stratification (HCS) and convolute beds are interpreted as upper shoreface zone (Table 1; Borgovini, 2003; Demory et al., 2011). Facies C consists of fine siltstone to marls rich in mollusk (bivalves and gastropods), benthic and rare planktonic foraminifera as *Globigerinoides trilobus*, *Globigerinoides altiaperturus* and *Catapsydrax dissimilis* and echinoderms, corals and bryozoans. The absence of high-energy sedimentary structures, the presence of marls to fine grain siltstones and the biotic association picture restricted marine conditions in an upper shoreface environment (Table 1; Fig. 3B7 and B8). The carbonated facies D1 is mainly composed of broken and disarticulated bioclats indicating intense reworking and high-energy conditions in shoreface environment (Table 1; Nalin et al., 2010). The D2 is composed of coral carpets and patches surrounded by bioclastic packstones (Table 1; Fig. 3B5 and B6; Riegl and Piller, 2000). The coral buildups and the bioclastic limestones are interpreted as deposited in a shallow high-energy platform setting (Demory et al., 2011).

4.1.2. Castillon-Du-Gard outcrop

The sedimentology and stratigraphy of Middle Miocene succession of Castillon-Du-Gard Sub-basin are revisited in Reynaud et al. (2012). In this study, the authors propose that the succession of shallow cool-water carbonates (e.g. Castillon Molasse, Langhian-Serravallian stages) alternates with offshore marls (e.g. Blue Marls, Burdigalian stage). Blue Marls, close to the contact with the Vers unit are grainier and characterized by wave ripples in sands and mollusk and foraminifera packstones (Molechfor; Reynaud et al., 2012). The biotic components composed of molechfor and bryozoans and the wave ripples testify to proximal offshore environment deposited in a low energy bay environment (Reynaud et al., 2012). Vers unit (part of Castillon Molasse sub-unit) shows an erosional surface with the blue marls that indicates decreasing accommodation space. This part of Castillon Molasse is a packstone/rudstone with abundant bivalves and bryozoans (Bryomol; Reynaud et al., 2012). This succession corresponds to shallow tidal deposits in a protected bay environment (Reynaud et al., 2012). Castillon unit (part of Castillon Molasse sub-unit) is a floatstone composed of bryozoan, mollusks and algae (Bryomol; Reynaud et al., 2012), interpreted as subtidal dunes in a sand sheet deposited in deeper marine environments than the Vers Unit. The top of this Castillon unit is a fine-grained packstone with bryozoans and mollusks (Bryomol; Reynaud et al., 2012) infilling successive channels and is interpreted as a decreasing water-depth with no emersion (Reynaud et al., 2012).

4.1.3. Age model

The age model proposed for Carry-Le-Rouet is based on a biostratigraphic study (Oudet et al., 2010) and a magnetostratigraphic one (Demory et al., 2011). Based on these two dating methods, we propose ages for each stratigraphic level markers on Carry-Le-Rouet section. Reefal unit (UR1 at 20 m) is estimated at 23.03 Ma and marks the

Table 1
Facies and depositional environments of Carry-Le-Rouet section.

Facies	Non-biotic elements		Biotic components	Matrix	Sedimentary structures	Environments
A1. Marls to fine siltstones	Rhizo-concretion, root traces			Clayey silts		Palaeosoils, Floodplain
A2. Conglomerates	Monogenic	Clasts source: Rudist Limestone (Barremian of the Nerthe)		Heterogeneous and clast-supported conglomerates with a sandstone matrix	Erosional base of decimetric to meter large channels	Fluviatile
	Poligenic	Clasts source: Rudist Limestones (Barremian of the Nerthe) and Paleozoic rocks				
A3. Conglomerates	Polygenic conglomerate with clasts composed of Rudist Limestones (Barremian of the Nerthe) and Paleozoic rocks		Rare bivalves and gastropods			Proximal deltaic domain
A4. Sandstones	Quartz grains, feldspath		Rare bivalves and gastropods	Calcareous sandstone	Continuous cm-thick beds intercalated with oyster and bioturbated sandstones	Distal deltaic lobes, transitional continental to marine
B1.Sandstones with conglomerates	Sandstones with quartz		Common bivalves, gastropods and barnacles	Fine grain sandstones	Planar stratification Bioturbation	Upper shoreface
B2. Fine to croase sandstones	Quartz grains		Abundant bivalves Common gastropods Rare wood fragments and bryozoans	Fine grain sandstones	Megaripples, HCS (Hummocky cross stratification), Convolute beds, Bioturbation	Lower shoreface
C. Siltstones to marls	Quartz grains		Common wood fragments and foraminifera Rare bivalves	Silt and Marls	Bioturbation (*Thallassinoïdes / Planolites*), HCS	Lagoon, protected environments
D1. Bioclastic packstones	Quartz grains		Abundant bivalves, gasteropods and corals Common bryozoans and echinoids	Broken bioclastic grains and micritic matrix	Bioturbation	Upper to lower shoreface
D2. Coral-rich floatstones to framestones	Floatstones	Reworked corals, and fragmented bioclasts	Abundant corals Common bivalves, gasteropods and bryozoans		Bioturbation, bioerosion, lenticular bioclastic accumulation and sigmoid reefal units	Lower shoreface
	Framestones	In situ corals, embedded in a bioclastic matrix				

Chattian-Aquitanian boundary. Reefal unit (UR2 at 25 m; Fig. 3A) is dated at 22.9 Ma. Turritellid-rich level (at 42 m, Fig. 3) is dated at 22.27 Ma. Finally, two reefal units UR3 (at 61 m; Fig. 3A) and UR4 (at 66 m; Fig. 3A) are respectively dated at 21.01 Ma and 21.00 Ma. Tamaris unit has only been dated by biostratigraphy with an age of 18.10 Ma at the base and 16.50 Ma at the top (Fondecave-Wallez et al., 1986). According to the literature, this unit is overlaid by two Langhian bars (Anglada et al., 1988; Arnaud et al., 1988; Oudet et al., 2010). An age of 15.97 Ma (Burdigalian-Langhian boundary) is proposed for the base of these bars.

For Castillon-Du-Gard outcrop, transition between Uzès Molasse and Blue Marls (base of the section) is dated at 15.97 Ma (Burdigalian-Langhian boundary). The Langhian-Serravallian boundary (~13.82 Ma) is located within the Castillon Molasse (Reynaud et al., 2012), despite limitation concerning available datation, we propose a position between 24 and 28 m.

4.2. Bivalve oxygen isotope composition

Along the sedimentary succession at Carry-Le-Rouet, the bivalve $\delta^{18}O$ values display relatively large scattering of about 4‰ within the same stratigraphic level (Fig. 4; Suppl. Table 1). Similar scatter amplitudes are found within single oyster shells (e.g., level 21A). Samples from the Chattian and Aquitanian stages yield $\delta^{18}O$ values ranging between about −4 and 0‰. By contrast, samples from the Burdigalian stage yield more positive $\delta^{18}O$ values ranging between about −3 and 1‰. The youngest Late Burdigalian level yields more negative $\delta^{18}O$ values than the rest of the Late Burdigalian stage.

Analyses performed on the largest oyster shells reveal different patterns of intra-shell $\delta^{18}O$ variability. Two shells present a sinusoidal signal with an amplitude of $\delta^{18}O$ variations up to ~ 4‰ (Fig. 5D and E). Two other shells present variations in $\delta^{18}O$ values with an amplitude of about 3‰, that could recall a sinusoidal pattern with a truncation of the highest $\delta^{18}O$ values (Fig. 5A and C). Two shells present a decrease in $\delta^{18}O$ values down to a plateau, followed by an increase, with an amplitude of variation of 1‰ (Fig. 5F) and 3‰ (Fig. 5B). A last shell presents more erratic variations in $\delta^{18}O$ values, within a ~1‰ range (Fig. 5G). For hinges that were sampled with a high spatial resolution, we observe a decrease in the amplitude of the signal between the Aquitanian (CAR17-6-28-a; CAR17-6-31base-a; CAR17-6-33-b and CAR17-6-33-c) and the Burdigalian (CAR17-8-43-h and CAR17-8-43-i), concomitantly with an overall increase in $\delta^{18}O$ values.

Similarly to the Carry-Le-Rouet section, $\delta^{18}O$ data from the Castillon-Du-Gard section present a large dispersion (Fig. 4B), slightly higher than at Carry-Le-Rouet as it reaches about 5‰ in the Castillon Molasse (9 to 17 m from the base of the section). $\delta^{18}O$ values seem to

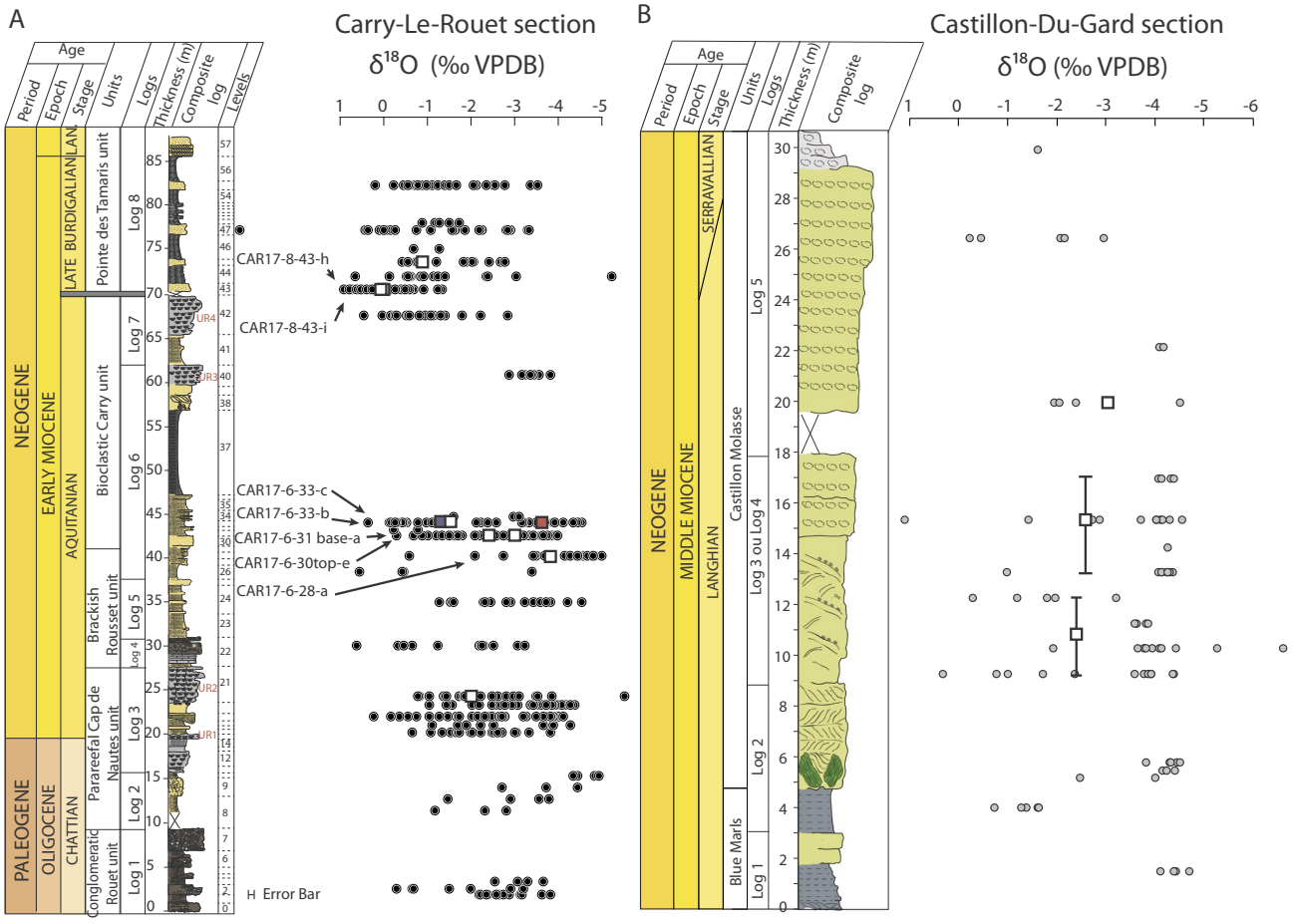

Fig. 4. Evolution of bivalve $\delta^{18}O$ throughout the section of Carry-Le-Rouet (A, Black plain circles) and Castillon-Du-Gard (B, Grey plain circles). Several microsamplings were realized per shells (levels where a microsampled oyster has been analyzed are identified by the name of the shell newt to the relevant data) and several shells were analyzed per stratigraphic levels. Each plotted data represents $\delta^{18}O$ data acquired in this work, including the multiple $\delta^{18}O$ measurements realized on some shells, appears on the figure. Analytical uncertainties are lower than the size of the circles (± 0.08‰, see Method section) and cannot be reported for each data point. Plain squares correspond to $\delta^{18}O_{shell}$ measured with clumped isotopes (White squares correspond to bulk of shell; Red square corresponds to summer part of shell CAR17-6-33-b; Blue square corresponds to winter part of shell CAR17-6-33). Vertical error bars reported on two Langhian samples, representing an uncertainty on the stratigraphic position of the samples, correspond to bulk shells that were gathered from stratigraphic levels newt to each other into a single analysis. (For interpretation of the references to colour in this figure legend, the reader is referred to the web version of this article.)

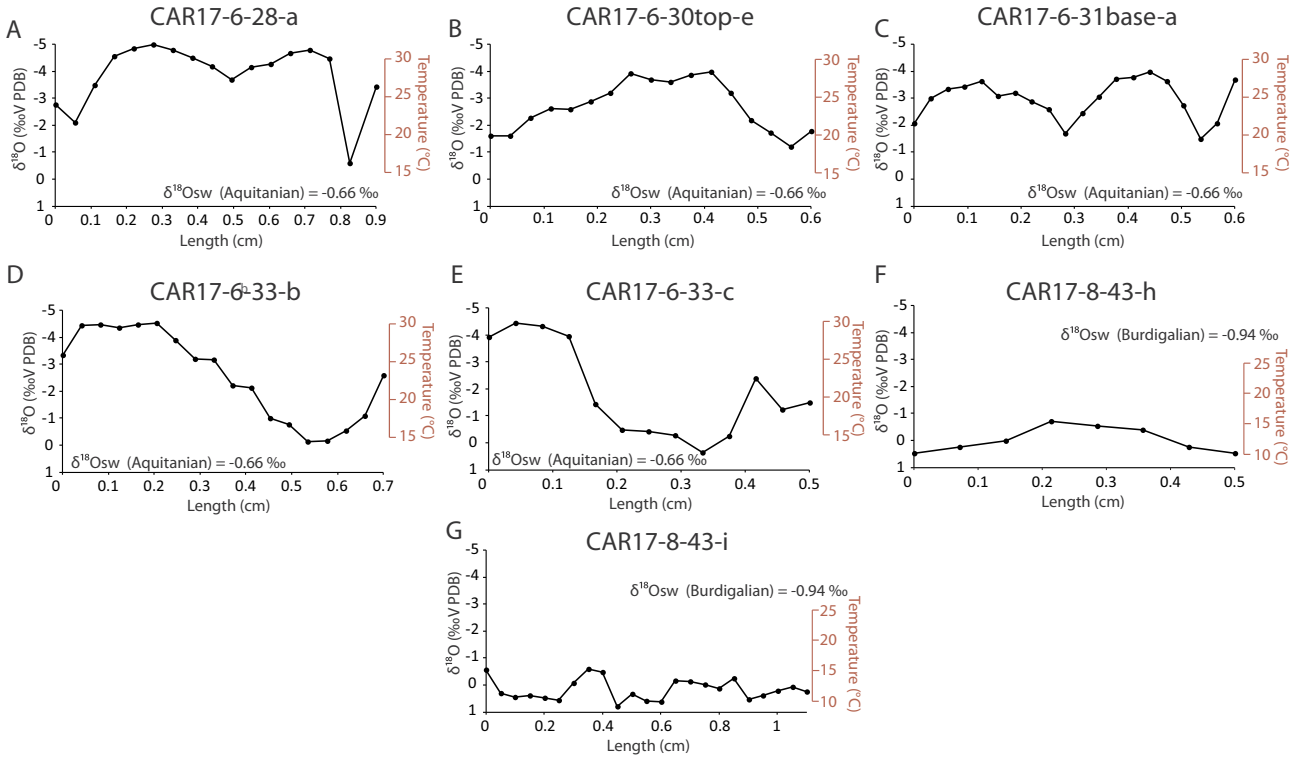

Fig. 5. Intra-shells $\delta^{18}O$ evolution from bivalves recovered from the Carry-Le-Rouet outcrop. A. CAR17-6-28-a; B. CAR17-6-30top-e; C. CAR17-6-31base-a; D. CAR17-6-33-b; E. CAR17-6-33-c; F. CAR17-8-43-h; G. CAR17-8-43-i. Corresponding temperatures have been calculated using the equation of Anderson and Arthur (1983) and a $\delta^{18}O_{sw}$ of −0.66‰$_{VPDB}$ (Billups and Schrag, 2002) for the Aquitanian (A to E) and of −0.94‰ $_{VPDB}$ (Billups and Schrag, 2002) for the Late Burdigalian (F and G). The error bar that applies to $\delta^{18}O$ measurements corresponds to the analytical reproducibility specified in the Method part, of ± 0.08‰.

increase at the top of the section, from average values of about −3.16‰ at about 20–22 m from the base of the section to average $\delta^{18}O$ values around −1.57‰ at about 27–30 m from the base of the section.

4.3. Bivalve clumped isotope analyses

The Δ_{47} values were measured on 12 bivalves and range between 0.676 and 0.716‰ (Table 2). They are not constant over time but fluctuate along the Carry-Le-Rouet and Castillon-Du-Gard sections. The 5 analyzed Aquitanian samples present Δ_{47} values comprised between 0.6852 ± 0.0093‰ and 0.705 ± 0.0095‰. One shell from the Aquitanian was large enough to provide two subsamples (CAR17-6-33-b), one sampled in the part yielding maximum $\delta^{18}O$ values from the microsampling approach, and the other in the part yielding minimum $\delta^{18}O$ values (Fig. 5D). Both subsamples give quite close Δ_{47} values of 0.6821 ± 0.01‰ and 0.6823 ± 0.0099‰. The 3 analyzed Burdigalian samples yield lower values (*p*-value of 0.08 based on a *t*-test), ranging from 0.6762 ± 0.0093‰ and 0.6882 ± 0.0093‰. The 3 analyzed Langhian samples display the highest values of the studied interval, ranging from 0.6968 ± 0.0098‰ and 0.7137 ± 0.0099‰ (higher than the Burdigalian samples: p-value of 0.04 based on a *t*-test; and higher than the Aquitanian samples: p-value of 0.12 based on a *t*-test).

Table 2
Δ_{47} data for all analyzed samples and conversion to temperature according to Peral et al. (2018) equation. Analytical errors reported here are derived from the external reproducibility of carbonate standards (N = 47) and samples (N = 39) within each analytical session, and conservatively account for the uncertainties in raw Δ_{47} measurements as well as those associated with the conversion to the "absolute" Δ_{47} reference frame. Local $\delta^{18}O_{sw}$ values were calculated using Δ_{47}-derived temperatures and $\delta^{18}O_{shell}$ with Anderson and Arthur (1983) equation. Salinity estimations derives from calculated local $\delta^{18}O_{sw}$ values, from which the $\delta^{18}O_{sw}$ of the global ocean (from Billups and Schrag, 2002) has been substracted, and Railsback and Anderson (1989) equation based on North Atlantic Ocean.

Age (m.y)	Sample	N	Seasonality	$\delta^{18}O_{shell}$ (‰$_{VPDB}$)	Δ_{47} (‰, ± 1 σ_E)	T (°C)	$\delta^{18}O_{sw}$ calculated (‰$_{VSMOW}$)	$\delta^{18}O_{sw}$ (Billups and Schrag, 2002) (‰$_{VPDB}$)	Salinity (‰)
22.9	CAR17_4_21A_a_B1	3	Bulk	−2.02	0.6903 ± 0.0093	19.9 ± 2.8	−1.06 ± 0.68	−0.66	34.3 ± 1.1
22.3	CAR17_6_28_a_B1	3	Bulk	−3.79	0.705 ± 0.0095	15.6 ± 2.7	−3.9 ± 0.65	−0.66	29.6 ± 1.1
22.2	CAR17_6_30TOP_B1	2	Bulk	−2.37	0.6934 ± 0.0097	19 ± 2.9	−1.68 ± 0.7	−0.66	33.3 ± 1.2
22.2	CAR17_6_31BASE_a_B1	3	Bulk	−2.96	0.6852 ± 0.0093	21.5 ± 2.9	−1.67 ± 0.7	−0.66	33.3 ± 1.2
22.1	CAR17_6_33_b_S1	3	Summer	−3.58	0.6821 ± 0.01	22.4 ± 3.1	−2.05 ± 0.75	−0.66	32.7 ± 1.3
22.1	CAR17_6_33_b_W1	3	Winter	−1.3	0.6823 ± 0.0099	22.4 ± 3.1	0.25 ± 0.75	−0.66	36.5 ± 1.3
22.1	CAR17_6_33_c_B1	3	Bulk	−1.53	0.6986 ± 0.01	17.5 ± 3	−1.14 ± 0.72	−0.66	34.2 ± 1.2
18.1	CAR17_8_43_h_B1	3	Bulk	0	0.6801 ± 0.0093	23.1 ± 2.9	1.71 ± 0.70	−0.94	39.4 ± 1.2
18.1	CAR17_8_43_i_B1	3	Bulk	0.12	0.6882 ± 0.0093	20.5 ± 2.8	1.19 ± 0.68	−0.94	38.5 ± 1.1
17.7	CAR17_8_45_a_B1	3	Bulk	−1.13	0.6762 ± 0.0093	24.3 ± 2.9	0.9 ± 0.70	−0.94	38.1 ± 1.2
14.9	CDG18_3&4_BASE_B1	3	Bulk	−2.37	0.7157 ± 0.0099	12.5 ± 2.8	−3.25 ± 0.68	−0.71	30.8 ± 1.1
14.6	CDG18_3&4_TOP_B1	3	Bulk	−2.59	0.7137 ± 0.0099	13.1 ± 2.8	−3.3 ± 0.68	−0.71	30.7 ± 1.1
14.2	CDG18_5_1_B1	3	Bulk	−2.98	0.6968 ± 0.0098	18 ± 2.9	−2.52 ± 0.70	−0.71	32 ± 1.2

Table 3
$^{87}Sr/^{86}Sr$ ratios of bulk carbonate and their error bars.

Age (m.y)	Sample	Nature	$^{87}Sr/^{86}Sr$	+ 2 σ_E
22.9	CAR17_4_21A_a_B1	Bulk	0.708255	0.000005
22.3	CAR17_6_28_a_B1	Bulk	0.708299	0.000007
22.2	CAR17_6_30TOP_B1	Bulk	0.708289	0.000005
22.2	CAR17_6_31BASE_a_B1	Bulk	0.708266	0.000005
22.1	CAR17_6_33_b_B1	Bulk	0.708228	0.000005
22.1	CAR17_6_33_c_B1	Bulk	0.708271	0.000009
18.1	CAR17_8_43_h_B1	Bulk	0.708696	0.000005
18.1	CAR17_8_43_i_B1	Bulk	0.708673	0.000006
17.7	CAR17_8_45_a_B1	Bulk	0.708695	0.000005
14.9	CDG18_3&4_BASE_B1	Bulk	0.708873	0.000005
14.6	CDG18_3&4_TOP_B1	Bulk	0.708868	0.000006
14.2	CDG18_5_1_B1	Bulk	0.708849	0.000005

4.4. $^{87Sr/86}Sr$ ratios

$^{87}Sr/^{86}Sr$ ratios range between 0.708222 and 0.708816 (Table 3). The strontium ratio average for the Aquitanian is 0.708237, 0.708655 for the Late Burdigalian and 0.708830 for Langhian stage. $^{87}Sr/^{86}Sr$ data increase about 600 ppm over the Aquitanian to Langhian time period.

5. Discussion

5.1. Intra-shell variability of oyster clumped and oxygen isotope composition

Modern oysters and other bivalves often present growth cessation during part of the year, when environmental conditions become stressful, due to extreme temperature, nutrient availability, or seawater oxygenation (Brown and Hartwick, 1988; Mitchell et al., 2000; Surge et al., 2001; Schöne, 2008; Ullmann et al., 2013; Huyghe et al., 2019) and can also occur during reproduction (Clark et al., 1974, Paulet et al., 2006). The growth cessation can result in an incomplete seasonal record of environmental parameters, namely temperature and seawater $\delta^{18}O$ ($\delta^{18}O_{sw}$), archived in the carbonate $\delta^{18}O$ signal of the shells (Ullmann et al., 2010). Growth cessation is apparent in shells CAR17-6-28-a and CAR17-6-31base-a (Fig. 5A and C), showing a truncated $\delta^{18}O$ signal at maximum $\delta^{18}O$ values. Therefore, only minimum amplitude of seasonal variations in environmental parameters can be obtained in these shells, along with temperature and $\delta^{18}O_{sw}$ during summer (represented by minimum carbonate $\delta^{18}O$ values, that are not truncated). We estimate that only 4 oysters may provide an estimation of the full amplitude of seasonal temperature and $\delta^{18}O_{sw}$ variations (Fig. 5 B, D, E, F). Other shells either present a truncated signal at maximum $\delta^{18}O$ values, or may not have lived long enough to record a complete seasonal cycle. Alternatively, it cannot be excluded that some shells (CAR17-8-43-I; Fig. 5G for instance) had a very low growth rate and that the sampling resolution was not accurate enough to allow to identify the seasonal pattern.

We have first estimated temperature variations using the standard approach based on carbonate $\delta^{18}O$ only, using the Anderson and Arthur (1983) equation established for calcitic molluscs with the $\delta^{18}O_{sw}$ reconstructed by Billups and Schrag (2002), of −0.66‰ for the Aquitanian, and of −0.94‰ for the Burdigalian. We have first considered a constant $\delta^{18}O_{sw}$ throughout the year to calculate the amplitude of seasonal temperature variations (ΔT) from $\delta^{18}O$ values for the 4 largest micro-sampled oysters devoid of truncation in the $\delta^{18}O$ signal (Fig. 5, B, D, E and F). The obtained ΔT with this approach range between 10 and 15 °C for the Aquitanian (Fig. 5, B, D and E) and around 5 °C for the Late Burdigalian (Fig. 5, F). This approach would thus show a ΔT decrease of 5 to 10 °C between the Aquitanian and the Late Burdigalian, along with a marked decrease in summer temperatures, of about 15 °C. Pollen assemblages indicate a temperate climate characterized by humid winters and drier summers in Europe during the Late Burdigalian (Jiménez-Moreno et al., 2010; Bruch et al., 2011). Such a climate would likely result in seasonal variations of local $\delta^{18}O_{sw}$ as well, with a higher $\delta^{18}O_{sw}$ during summer and a lower $\delta^{18}O_{sw}$ during winter. Taking these suspected seasonal variations of $\delta^{18}O_{sw}$ into consideration would lead to increased estimates of seasonal temperature amplitude variations compared to those calculated using a constant $\delta^{18}O_{sw}$.

By comparison, the seasonal temperature contrast calculated from $\delta^{18}O$ variations measured within Late Burdigalian oyster shells from Central Europe (Harzhauser et al., 2011), also considering a constant $\delta^{18}O_{sw}$ throughout the year, is much higher (~ 10 °C) as part of another study. Summer temperatures calculated by these authors are also quite high at ~ 28 °C, but close to the temperatures calculated from our Aquitanian oyster shells. Harzhauser et al. (2011) report winter temperatures at ~9–10 °C similar those obtained in this study for the Late Burdigalian stage. This seasonal difference between the Aquitanian and the Late Burdigalian may be explained by a microclimate on the Northwestern Mediterranean Sea margin during the Late Burdigalian, or by different seasonal variations in salinity between the two regions, as the oysters collected in Harzhauser et al. (2011) study come from estuarine environments where the salinity is around 23‰. The Carry-Le-Rouet and Castillon-Du-Gard latitude changed very little since the early Miocene at ~ 43°N (Jolivet et al., 2006). At present, the annual water at 10 m water depth in the Gulf of Lion is around 18 °C fluctuating between winter temperatures of 13 ± 1 °C and summer temperatures of 23 ± 2 °C (Data from Levitus94; Levitus and Boyer, 1994). This seasonal temperature variation of ~10 °C is quite similar to our estimates for the Aquitanian stage, although the temperatures calculated for this stage are globally higher. By contrast, the Late Burdigalian seasonal contrast estimates are much weaker compared to current one, with in addition cooler summer (~10 °C) and winter (~15 °C) temperatures. This differs significantly from increasing temperatures recorded worldwide at this period that marks the initiation of the climate warming leading to the MMCO during the Langhian (Zachos et al., 2008; Jiménez-Moreno et al., 2010; Harzhauser et al., 2011).

An attempt was made to estimate seasonal seawater temperature contrast independently from variations in $\delta^{18}O_{sw}$, based on clumped isotopes. Using conventional $\delta^{18}O$ measurements, complete seasonal cycles in temperature and $\delta^{18}O_{sw}$ may be identified in 4 oysters (Fig. 5 B, D, E and F) allowing to identify which part of the shells mineralized during summer (minimum $\delta^{18}O$) versus winter (maximum $\delta^{18}O$), and these inferred seasonal extrema were then sampled for Δ_{47} analyses. Unfortunately, due to the amount of material required per Δ_{47} analysis and the small size of shells, only one Aquitanian shell (CAR17-6-33-b, Fig. 5D) could be used, providing two sub-samples corresponding to the $\delta^{18}O$ minimum and maximum, respectively (all other shells provided "bulk" shell material assumed to reflect weighted average annual temperatures, and the corresponding results are presented in Section 5.2.1).

There is today a large body of literature pertaining to the calibration of clumped-isotope thermometry in biogenic and inorganic carbonates. Among other reasons, this is due to the lingering methodological issues which have so far hindered precise inter-laboratory comparisons (e.g., Petersen et al., 2019 and references therein). Here we opt for the recent calibration by Peral et al. (2018), for two main reasons. For one thing, that study was performed at LSCE using identical methods and instruments as those reported here. In addition, despite the Peral et al., 2018 calibration being based on foraminifera, published and unpublished results from LSCE yield a calibration function for modern oysters and pectens, which is virtually identical to that of Peral et al. (2018).

The two "seasonal" sub-samples (CAR17-6-33-b-S1 and -W1) yield $\delta^{18}O$ values of −3.6‰ and −1.3‰ respectively (Table 2), consistent with those obtained through microsampling (Fig. 6, Areas 1–2). Somewhat surprisingly, the corresponding Δ_{47}-derived temperatures (Fig. 6) are statistically indistinguishable (22.4 ± 3.1 °C versus 22.4 ± 3.1 °C, 1 σ_E). If these temperatures are used with the $\delta^{18}O$

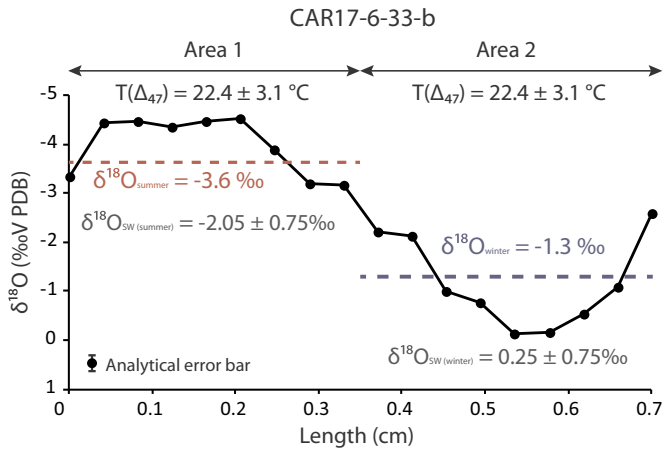

Fig. 6. Distribution of $\delta^{18}O$ values along CAR17-6-33-b umbo obtained from microsampling (black plain circles). The dotted red and blue lines represent the $\delta^{18}O$ values of the two samples recovered from this oyster for Δ_{47} analyses, over the length of the shell corresponding to minimum $\delta^{18}O$ values and maximum $\delta^{18}O$ values, respectively, as described in the text (Part 3.3). The temperature calculated from Δ_{47} ($T(\Delta_{47})$) is reported for these two samples. The error bar that applies to $\delta^{18}O$ measurements corresponds to the analytical reproducibility specified in the Method part, of ± 0.08‰. (For interpretation of the references to colour in this figure legend, the reader is referred to the web version of this article.)

values of the two shell subsamples and the equation of Anderson and Arthur (1983), the resulting $\delta^{18}O_{sw}$ calculated are of −2.05‰ and 0.25‰ for the parts of the shell yielding minimum and maximum $\delta^{18}O$ values, respectively. The absence of seasonal temperature variation appears unlikely considering the paleolatitude of the Carry-Le-Rouet site during the Aquitanian (~10 °C seasonality at this latitude at present time), and considering independent estimates based on pollen data that point to the existence of seasonal variations around 20 °C in atmospheric temperature in Europe (Akgün et al., 2007). This oyster shell yields the highest Δ_{47}-derived temperatures for the Aquitanian, 3 °C higher than the other analyzed shells (Table 2). As summer tend to be the period with the highest growing rate in oysters from subtropical to temperate settings, it is possible that the intra-shell $\delta^{18}O$ record defined with the microsampling method actually reflects a much shorter time span of the oyster life than a year. The large variations in $\delta^{18}O$ recorded within the oyster shell could then reflect punctual freshwater discharges within the same season. This sample has been recovered from level 33, located at the transition between the Brackish Rousset Unit and the Bioclastic Carry Unit (Demory et al., 2011). The presence of brackish conditions in the lower part of the Bioclastic Carry Unit is supported by the presence of wood fragments and reworked potamids, pointing to the existence of punctual freshwater discharges in the shallow marine deposits of the Bioclastic Rousset unit.

5.2. Miocene climate change in Mediterranean area

5.2.1. Comparison between bivalve $\delta^{18}O$ values and benthic foraminifera $\delta^{18}O$

Bivalve $\delta^{18}O$ values present a large dispersion within each stratigraphic level, typically around 4‰. As shown by the microsampling realized on sections of the largest oysters (Fig. 5) that presents one seasonality-cycle at most, most of the analyses performed on bivalve fragments likely represent a relatively short time of the bivalve life, shorter than a year and even maybe than a season. Thus, part of this large dispersion is likely to arise from seasonal or intra-seasonal variations in temperature and $\delta^{18}O_{sw}$, as a bivalve fragment can have been built mostly during a winter while another fragment recovered from the same stratigraphic level may have formed mostly during summer. Due to this large dispersion, we applied a statistical treatment to the dataset in order to identify significant climatic trends in the signal, using the SiZer package (Sonderegger and Sonderegger, 2018) in the R software (R Core Team, 2017). The «SiZer» statistical method (based on studying statistical Significance of ZERo crossings of smoothed estimates; Marron and Chaudhuri, 1998) has been widely used on paleoclimatic proxies such as carbonate $\delta^{18}O$ values (increasing or decreasing) to detect significant climatic trend at different timescales (Weckström et al., 2006; Dera et al., 2011; Bougeault et al., 2017). This method is based on the construction of curves fitting time series using different level of smoothing (h). The first derivatives of each curve are simultaneously computed with their 95% confidence intervals, allowing the signs of derivative estimated to be statistically tested. If the sign of the first derivative is different from 0, including entire 95% confidence interval, then the corresponding trend shows a significant increase (for a positive sign of the first derivative) or a significant decrease (for a negative sign of the first derivative). These multiple tests are then represented as a map to identify the trend significance for each size of smoothing. When the result is significant, it is coded in blue if it is positive and in red if it is negative. On the contrary, it is coded in grey if it does not differ from 0 and white when data are not numerous enough to identify significant trends ($n < 5$). A Sizer map can thus be viewed as the summary of a large number (hundreds) of hypothesis test results, with each pixel of the map representing the result of a hypothesis test where the null hypothesis corresponds to the 0 slope. More formally, these tests are obtained from confidence interval calculations using the row-wise method that is detailed in Hannig and Marron (2006).

In this study, SiZer maps have been generated using a bandwith h comprised between 0.1 and 10 Myrs (Fig. 7). This statistical treatment applied on carbonate $\delta^{18}O$ data highlights the existence of a long-term increase in $\delta^{18}O$ values between 23 and 20 Ma followed by a long-term decrease between 18 and 15 Ma. A second increase of $\delta^{18}O$ values is depicted as well during the Serravallian, but over shorter timescales of about 1 to 2 Myrs. Using the equation of Anderson and Arthur (1983) and a $\delta^{18}O_{sw}$ (Table 2) published by Billups and Schrag (2002), as described in Section 5.1., these trends in $\delta^{18}O$ values depicted by the SiZer map would correspond to (1) a cooling of about 10 °C, from temperatures of about 25 °C in the Chattian and earliest Aquitanian to about 15 °C in the Late Burdigalian, (2) a warming of about 12 °C, with temperatures up to 27 °C on average during the Langhian, and (3) a shorter-time cooling of about 4 °C, with temperatures down to 23 °C during the Serravallian (Fig. 8A). Note that the $\delta^{18}O$ signal only depicts the cooling initiation that likely continues further into the Serravallian.

Our new dataset recovered from shallow coastal environments presents some similarities with the evolution of benthic foraminifera $\delta^{18}O$ ($\delta^{18}O_{bf}$; Zachos et al., 2008; Fig. 7). From the Chattian to the Burdigalian, the $\delta^{18}O$ increase highlighted by the SiZer map (Fig. 7) is coherent with the general increasing trend of $\delta^{18}O_{bf}$ values from the latest Oligocene to the Burdigalian, although our dataset is not continuous enough to identify the shorter-time Mi-events as evidenced in former studies (Zachos et al., 2008; Mawbey and Lear, 2013; Beddow et al., 2016). The $\delta^{18}O$ minimum identified in our dataset during the Langhian could well correspond to the MMCO (Zachos et al., 2008; Mawbey and Lear, 2013; Beddow et al., 2016; Goldner et al., 2014; Holbourn et al., 2015; Super et al., 2018) detected in the $\delta^{18}O_{bf}$ dataset, while the $\delta^{18}O$ increase at the top the Castillon-Du-Gard succession could correspond to the initiation of the MMCT (Zachos et al., 2001; Billups and Schrag, 2002; Shevenell et al., 2004).

In contrast, the amplitude of the $\delta^{18}O$ variations is much larger in our bivalves recovered from coastal environments compared to the deep marine environment record. The Early Miocene cooling is expressed by an increase of 0.5‰ of the $\delta^{18}O_{bf}$ in deep marine environment (Fig. 7) while the amplitude depicted by bivalve $\delta^{18}O$ at Carry-le-Rouet is four times higher. Similarly, for the MMCO, the $\delta^{18}O_{bf}$ decreases by about 1‰ but about 2.5‰ in our bivalve shells living in proximal environments. This amplitude difference is however expected

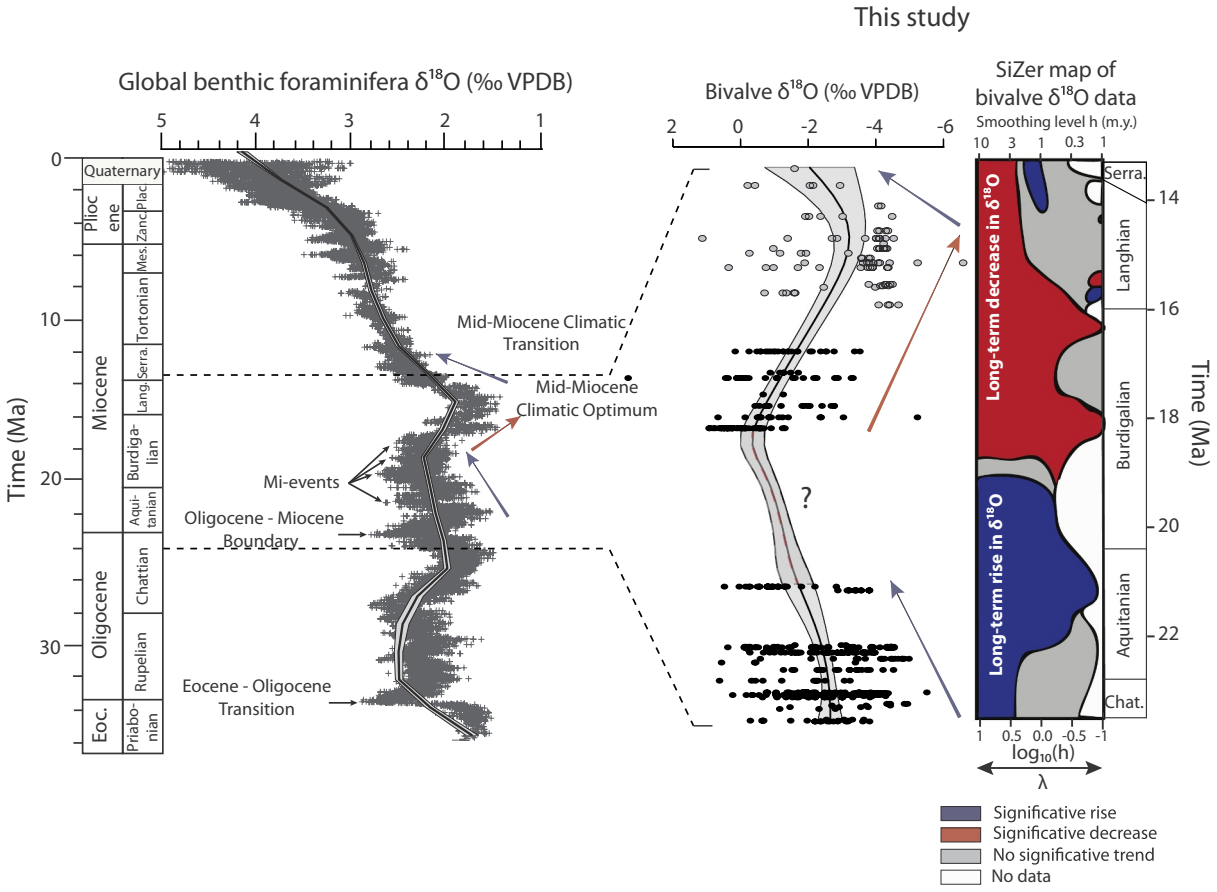

Fig. 7. Comparison of geochemical data from bivalve shells obtained in this work, with the results of the applied statistical treatment (SiZer Map: 0.1 < h < 10 Myrs; Blue: significant increase; Red: significant decrease; Grey: No significant; White: No data), with the benthic foraminifera $\delta^{18}O$ global record (Zachos et al., 2008). Black plain circles correspond to bivalve $\delta^{18}O$ values for the Carry-Le-Rouet section and Grey plain circles correspond to bivalve $\delta^{18}O$ values from Castillon-Du-Gard. Smoothed black curves and their grey envelope on foraminifera $\delta^{18}O$ global record and on our bivalve $\delta^{18}O$ values are realized using *locally.weighted.polynomial* function (the confidence intervals are created using the row-wise method of Hannig and Marron, 2006) of SiZer Package (R software) with a bandwith "h" at 1 Ma for both curves. (For interpretation of the references to colour in this figure legend, the reader is referred to the web version of this article.)

as shallow marine environments record larger temperature variations than deep-sea environments during climate fluctuations. Both environments records variations in the ocean $\delta^{18}O$ linked to the waning and waxing of polar ice-sheets. In shallow coastal environments, an additional source of carbonate $\delta^{18}O$ variations is be related to the hydrological cycle, whose variability in time and space can impact local $\delta^{18}O_{sw}$. Sedimentary facies at Carry-Le-Rouet and Castillon-Du-Gard point to the persistence of an open marine depositional environment, except for the Tamaris section which presents sedimentary facies coherent with a more restricted bay environment (Fig. 3). Yet, even open marine environments are susceptible to be impacted by nearby runoff leading to salinity variations, especially in coastal environments. The sporadic occurrence of wood fragments and the low abundance of the fossils throughout the Tamaris section may point to nearby freshwater inputs. Such an impact of local seawater $\delta^{18}O$ fluctuations is further supported by the quite high temperatures of up to 35–40 °C (Fig. 8A), calculated from bivalve $\delta^{18}O$ using the equation of Anderson and Arthur (1983) and the $\delta^{18}O_{sw}$ of Billups and Schrag (2002) established for the global ocean, that most likely exceeded the tolerance of bivalves (Stenzel, 1971). Thus, we anticipate that part of the large variations recorded in the bivalve $\delta^{18}O$ signal may be related to change in the local hydrological cycle in response to global climate change occurring at this period.

5.2.2. Evolution of shallow seawater temperatures inferred from clumped isotope analyses

"Bulk" Δ_{47} analyses, representing averaged isotopic composition over at least part of the life span of the organisms (all shells except CAR17-6-33-b) could help decipher whether the bivalve $\delta^{18}O$ signal is related to variations in seawater temperature and $\delta^{18}O_{sw}$. The Δ_{47}-derived shallow seawater temperatures "T_{47}" (Table 2; Fig. 8A) range from 15.6 ± 2.7 °C to 22.4 ± 3.1 °C (1 σ_E), with an average of 19.7 ± 1.1 °C (1 σ_E, fully propagated from the analytical errors on individual samples) which is cooler (*p*-value of 0.003 using a *t*-test) than those calculated with the $\delta^{18}O_{shell}$ and a $\delta^{18}O_{sw}$ of Billups and Schrag (2002) for the Aquitanian (about 25 °C on average). Previous studies on pollen assemblages in Europe (Akgün et al., 2007) and of coral assemblages in the Mediterranean Sea (Bosellini and Perrin, 2008), argue for atmospheric temperatures between 16.5 and 21.3 °C and sea surface temperatures between 18 and 19.3 °C, respectively, during the Aquitanian stage. These values are in good agreement with the temperatures calculated from our Δ_{47} analyses.

For the Late Burdigalian stage, shallow seawater T_{47} values are higher (Table 2; Fig. 8A) than those for the Aquitanian (p-value of 0.048 using *t*-test), ranging between 20.5 ± 2.8 °C and 24.3 ± 2.9 °C (1 σ_E) and with an average of 22.6 ± 1.7 °C (1 σ_E). These Late Burdigalian temperatures calculated from Δ_{47} data are higher (p-value of 0.021 using a *t*-test) than those calculated from bivalve $\delta^{18}O$ using a

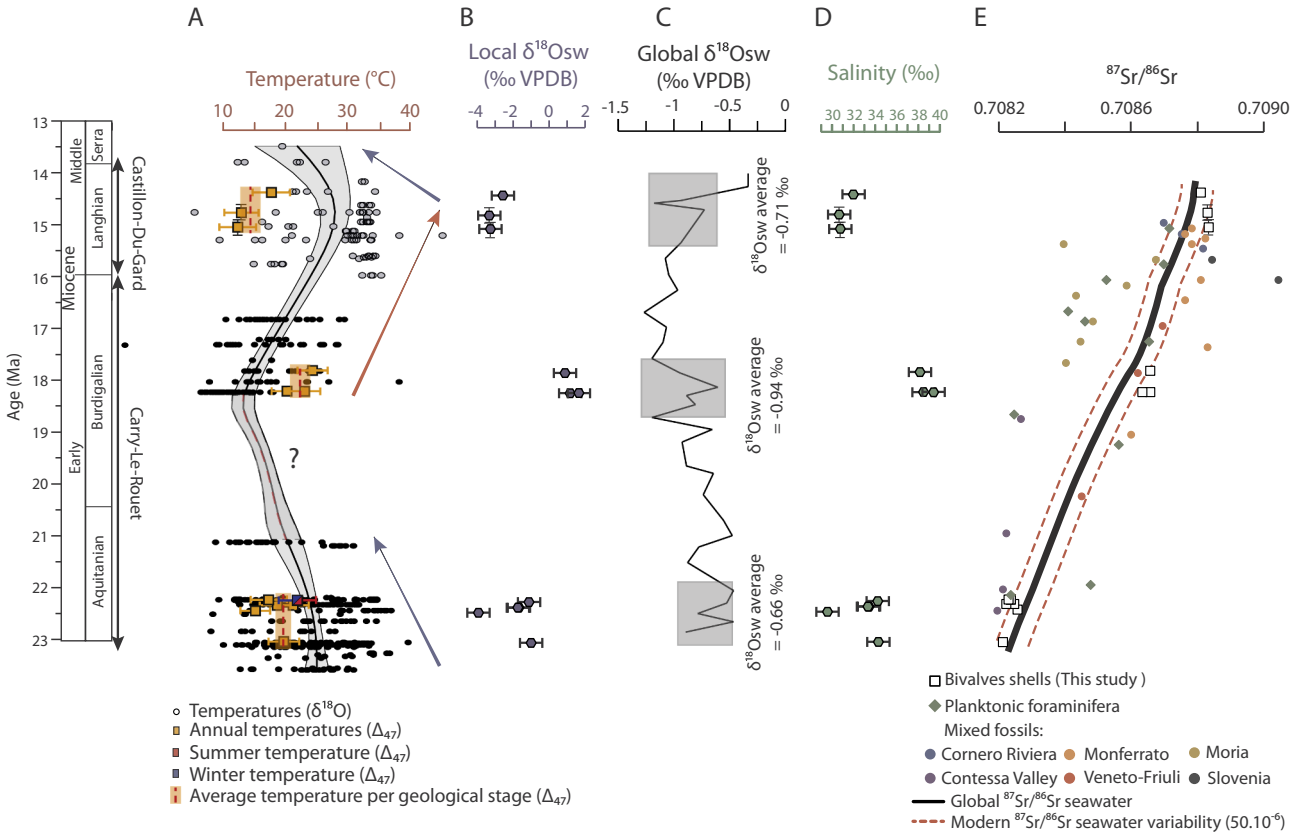

Fig. 8. A. Comparison between $\delta^{18}O$-derived temperatures and Δ_{47}-derived Temperatures. $\delta^{18}O$-derived temperatures are calculated using the $\delta^{18}O_{sw}$ from Billups and Scharg (2002) and the equation of Anderson and Arthur (1983) as described in the text, Sections 5.1 and 5.2.1. Black plain circles correspond to Carry-Le-Rouet section; Grey plain circles correspond to Castillon-Du-Gard Section. Vertical error bars reported on 2 bulk shells, representing an uncertainty on the stratigraphic position of the samples, correspond to bulk shells that were gathered from stratigraphic levels newt to each other into a single analysis. Black smoothed curve and associated grey interval have been realized using the *locally.weighted.polynomial* function with a bandwith "h" at 1 Ma. Δ_{47}-derived mean annual temperatures are estimated from clumped isotope analyses bulk shells using the equation of Peral et al. (2018): Orange squares: mean annual temperatures; Red square: summer seawater CAR17-6-33-b); Blue square: winter seawater temperatures (CAR17-6-33-b). Vertical error bars as for $\delta^{18}O$-derived temperatures. B. Evolution of local $\delta^{18}O_{sw}$ calculated from $\delta^{18}O_{shell}$ and Δ_{47}-derived temperatures using Anderson and Arthur (1983) equation (see Section 5.2.3 for further detail) C. Global $\delta^{18}O_{sw}$ curve, is from Billups and Schrag (2002). The shaded areas reported on this curve highlight the portions of the curve selected to calculate the average $\delta^{18}O_{sw}$ value of the global ocean for the three periods for which coupled Δ_{47}-$\delta^{18}O$ analyses have been performed on bivalves, with a minimum of 3 data of the curve gathered for the calculation. D. Salinity estimations are calculated using Railsback and Anderson (1989) equation based on North Atlantic Ocean and local $\delta^{18}O_{sw}$ values from which global ocean $\delta^{18}O_{sw}$ value has been subtracted (see Section 5.2.3 for further detail) E. Bivalve $^{87}Sr/^{86}Sr$ evolution (white squares) compared to the $^{87}Sr/^{86}Sr$ of the global ocean (black line; McArthur and Howarth, 2004) with the two red dashed lines showing the variability of ± 50 ppm recorded in the modern ocean (El Meknassi et al., 2018), and compared to published planktonic foraminifera (Cornacchia et al., 2018) and mixed fossils (Kocsis et al., 2008) $^{87}Sr/^{86}Sr$ from the North Western Mediterranean Sea. (For interpretation of the references to colour in this figure legend, the reader is referred to the web version of this article.)

$\delta^{18}O_{sw}$ from Billups and Schrag (2002), by about 15 °C on average, but are again in better agreement with those published in the literature (Lecuyer et al., 1996; Goedert et al., 2017). Indeed, with the exception of the slightly cooler temperatures deduced from coral assemblages for the Late Burdigalian (18.5 to 20.5 °C; Bosellini and Perrin, 2008), our temperature range is quite close to that deduced from combined analyses of marine mammal and fish tooth $\delta^{18}O$, that is comprised between 20 and 28 °C (Goedert et al., 2017) in the northern Aquitaine Basin, and between 18 and 22 °C in Brittany (Lecuyer et al., 1996).

For the Langhian stage, T_{47} values range from 12.5 ± 2.8 °C to 18 ± 2.9 °C (1 σ_E) with an average of 14.5 ± 1.6 °C (1 σ_E). Again, these Langhian temperatures derived from Δ_{47} data are cooler (*p*-value of 0.026 using a *t*-test), as for the Aquitanian (Table 2; Fig. 8A), than those calculated from bivalve $\delta^{18}O$ using a $\delta^{18}O_{sw}$ from Billups and Schrag (2002), of about 25 °C on average. These values might appear cooler than expected, considering that this period encompasses the MMCO for which both terrestrial and marine proxy data suggest globally warmer conditions relative to the Early Miocene, especially at mid- and high latitudes (Mosbrugger et al., 2005; Bruch et al., 2007; Bruch et al., 2011; Shevenell et al., 2008; Zachos et al., 2008; Super et al., 2018). On the other hand, our clumped-isotope results are coherent with atmospheric temperatures inferred from pollen assemblages on the northwestern Mediterranean margin (17–18 °C, Bruch et al., 2007), and in Germany (16–21 °C, Böhme et al., 2007). Published sea surface temperatures inferred from combined $\delta^{18}O$ analyses of mammals and fish remains, are around 20 °C ± 2 °C in Brittany (Lecuyer et al., 1996), slightly higher than our Δ_{47}-derived temperatures. Additional estimates, calculated from bivalve $\delta^{18}O$, range between 18 and 28 °C in the Tethyan domain (Harzhauser et al., 2011) and between 16.5 and 19.5 °C from coral assemblage (Bosellini and Perrin, 2008). Although the uncertainties associated with the calculation of all these temperatures are difficult to estimate, they all tend to appear quite lower than the 27–37 °C range obtained from TEX_{86} analyses at similar latitude in the central Atlantic (Super et al., 2018), similarly to our Δ_{47}-derived temperature estimates. Our new temperature data inferred from Δ_{47} analyses are thus coherent with the temperatures published in the literature for the Mediterranean and Tethyan regions and support lower temperatures in this general area during the MMCO compared to other sites at similar paleolatitude.

A relatively cool local to regional climate during the MMCO,

compared to that inferred from similar paleolatitudes based on TEX_{86} data, is also consistent with the high abundance of bryozoans throughout the Castillon-Du-Gard section. The proliferation of bryozoans, mainly in the form of encrusting cheilostomes, colonized the shallow seawater setting of the Rhodano-Provencal Sub-basins and has been interpreted as deposited in temperate to warm temperate depositional environment (Taylor and James, 2013). Similar bryozoan-rich deposits in the Tethyan domain have been interpreted as cool-water carbonates by Randazzo et al. (1999), based on $\delta^{18}O$ analyses and ecological reconstitutions. So far, such lower seawater temperatures in the Mediterranean and Tethyan regions have been tentatively explained by the deep cold-water arrivals coming from development of upwellings (Randazzo et al., 1999; Reuter et al., 2013).

Thus the temperatures obtained from Δ_{47} analyses are in relatively good agreement with those published in the literature in the general region, but quite markedly differ from those obtained from bivalve $\delta^{18}O$ using the equation of Anderson and Arthur (1983) and the $\delta^{18}O_{sw}$ of the global ocean of Billups and Schrag (2002). This apparent discrepancy between Δ_{47}-derived and $\delta^{18}O$ -derived temperatures, observed for the different studied periods, can be explained by modifications of the hydrological cycle linked to global climate change, leading to a departure of the local $\delta^{18}O_{sw}$ from that of the global ocean estimated by Billups and Schrag (2002).

5.2.3. Variations in the local hydrological cycle

In order to estimate the temporal evolution of the local $\delta^{18}O_{sw}$ we used the seawater temperatures inferred from Δ_{47} analyses together with the $\delta^{18}O$ values of the oyster shells measured on the same powder sample, and the Anderson and Arthur (1983) equation.

Our calculated values point to low local $\delta^{18}O_{sw}$ values during the Aquitanian (values ranging from −3.9 to −1.06‰ with an average of −1.89‰), that are likely to reflect enhanced precipitations and a lower salinity of the shallow neritic waters during this period (Table 2; Fig. 8B). For the late Burdigalian, the calculated $\delta^{18}O_{sw}$ are much higher (p-value of 0,021 using a *t*-test), ranging from 0.9 to 1.71‰ with an average of 1.27‰, that points to a decrease in precipitation and runoff and/or an increase in evaporation (Table 2; Fig. 8B). This finding agrees well with the display of a low floro-faunal content in the Late Burdigalian of the Tamaris succession, an absence of high-energy sedimentary structures and a deposition of fine-grain sediments, suggesting that the depositional environment was potentially more restricted. Our calculated $\delta^{18}O_{sw}$ values for the Late Burdigalian are close although slightly lower than the estimation of about 2‰ on average for coastal seawater in the nearby Aquitaine Basin during the Late Burdigalian by Goedert et al. (2017), based on combined $\delta^{18}O$ analyses of marine mammals and fish remains. The local $\delta^{18}O_{sw}$ values for the Langhian are again lower (ranging from −3.3 to −2.52‰, with on average of −3.02‰), which would point to enhanced precipitations and runoff during this period (Table 2; Fig. 8B). These values are significantly lower than those calculated for the Burdigalian (*p*-value of 0.0002 using a *t*-test). The Castillon-Du-Gard Sub-basin is located on the periphery of the main Rhodano-Provencal Basin, with the presence of nearshore facies (Bryomol) in the Castillon-Du-Gard area (Reynaud et al., 2012), indicative of a semi-enclosed basin, and of sediments organized in a regressive sequence. These conditions would further favor increased freshwater inputs into this Sub-basin in the case of an enhanced hydrological cycle. In addition, a tectonically-enhanced uplift of Alps chain occurred between the lower and the middle Miocene, that can induce changes in the drainage pattern, major fluvial incisions, and increased runoff in the Castillon-Du-Gard Sub-basin (Reynaud et al., 2012). In any case, following this coupled Δ_{47} - $\delta^{18}O$ approach, our results would then point to the existence of changes in the local hydrological cycle during the studied period, from the early to the middle Miocene. Importantly, changes in local $\delta^{18}O_{sw}$, likely driven by changes in freshwater inputs, dominate the recorded changes in bivalve $\delta^{18}O$, while temperature changes appear to have a more minor influence (Fig. 9A and B).

Part of the local $\delta^{18}O_{sw}$ evolution reconstructed from the coupled Δ_{47} and $\delta^{18}O$ analyses in this study is due to changes in the ocean $\delta^{18}O_{sw}$ at a global scale, linked to variations in ice-sheet volume on Antarctica at that time. In an attempt to estimate first-order variations in local salinity due to changes in the local hydrological cycle only, we subtracted to our calculated local $\delta^{18}O_{sw}$ the ocean $\delta^{18}O_{sw}$ (Fig. 8C) values published in Billups and Schrag (2002), i.e. -0.66‰ $_{VPDB}$ (or −0.86‰ $_{VSMOW}$; see Grossman (2012) for conversion from the VPDB to the VSMOW scale) for the Aquitanian, −0.94‰ $_{VPDB}$ (or − 1.14‰ $_{VSMOW}$) for the Burdigalian, and − 0.71‰$_{VPDB}$ (or − 0.91‰ $_{VSMOW}$) for the Langhian. We then used salinity - $\delta^{18}O_{sw}$ relations established in modern environments but still comparable to the sites investigated here. We chose for this rough approach the equation proposed by Railsback and Anderson (1989) based on modern surface North Atlantic Ocean salinity and $\delta^{18}O_{sw}$ data. A salinity - $\delta^{18}O_{sw}$ relation exists for the modern Mediterranean Sea (Pierre, 1999). However, during the Miocene the Mediterranean Sea was still largely open to the Atlantic Ocean on the west, and to the Indian Ocean on the east prior to its closure during the late Miocene (Jolivet et al., 2006; Do Couto et al., 2016). Therefore, we think that this configuration of the Mediterranean Sea during the Miocene, quite different than the modern one, likely impacted the salinity - $\delta^{18}O_{sw}$ relation. To our opinion, it is thus preferable to consider the equation of Railsback and Anderson (1989) based on surface North Atlantic data. Note that if the equation of Pierre (1999) had been used instead, the estimated salinities presented below would be of about 20 to 31‰ for the Aquitanian, about 40 to 43‰ for the Late Burdigalian and about 22 to 25‰ for the Langhian.

For the Aquitanian stage, the reconstructed salinities based on this approach tend to be lower on average than the mean value of 35‰ of the modern open ocean, with an important variability in the 30 and 34‰ range based on bulk shells, i.e. an average salinity throughout the bivalve life (Table 2; Fig. 8D). This points to a contribution of freshwater inputs to the local seawater by runoff, rainfall, or groundwater discharge, although this range remains within the tolerance of the stenohalin organisms (corals, bryozoans, echinoids and foraminifera) observed at Carry le Rouet during the Aquitanian (Oertli, 1964). The Sr isotope composition of bivalve shells can provide additional insights on potential freshwater inputs, if they are large enough to impact the local seawater Sr budget. The strontium isotope composition ($^{87}Sr/^{86}Sr$) of bio-carbonates reflects the isotopic composition of the water in which they form their test (Veizer et al., 1999; Palmer and Elderfield, 1985). Therefore, the $^{87}Sr/^{86}Sr$ ratios measured on carbonated organisms enable to reconstruct the isotopic signature of the aqueous environment in which they thrive.

The measured $^{87}Sr/^{86}Sr$ of the bivalves compares well with the Sr isotope signatures of planktonic foraminifera and of mixed calcitic fossils from the Umbria-March Basin (Fig. 8E; Kocsis et al., 2008; Cornacchia et al., 2018). Our Sr isotope record mostly falls within the global seawater Sr isotope reference curve (McArthur and Howarth, 2004), when considering a seawater $^{87}Sr/^{86}Sr$ variability comparable to that recorded in the modern ocean (± 50 ppm; El Meknassi et al., 2018). For the Aquitanian, the $^{87}Sr/^{86}Sr$ of our samples tends to fall at the lower limit of this range, and even presents slightly more unradiogenic values than that of the open ocean at that time, as observed from the nearby Umbria-March Basin (Kocsis et al., 2008; Fig. 8E). This slight deviation from the open ocean Sr isotope composition may derive from active volcanism in the region, that can release mantle-derived unradiogenic Sr signature into the local seawater and influence its Sr budget. Sporadic volcanic activity during the Miocene in the western Mediterranean Sea can indeed be generated during the extension of the Tyrrhenan and Algéro-Provencal basins (Frizon de Lamotte et al., 2000; Schettino and Turco, 2011; Bialik et al., 2019). Large eruptions within the 25–19 Ma interval are supported by volcanoclastic sediments in the vicinity of the studied region (from Provence to Sardinia and Corsica and in the Umbria-March Basin; Montanari et al., 1994; Beccaluva

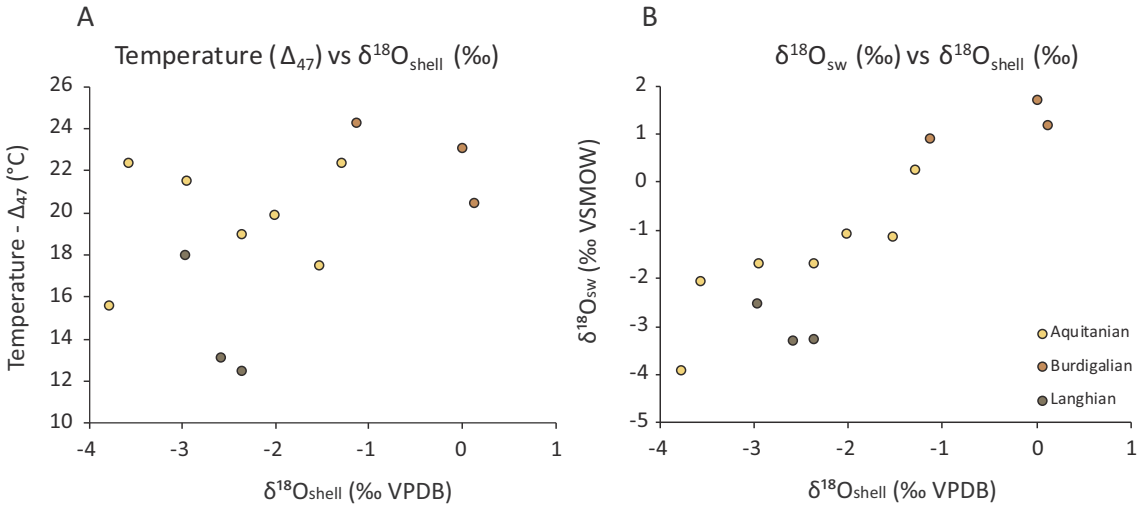

Fig. 9. A. $\delta^{18}O_{shell}$ values versus Δ_{47}-derived temperatures measured with clumped isotopes. B. Local $\delta^{18}O_{sw}$ values calculated with Anderson and Arthur (1983) equation versus $\delta^{18}O_{shell}$ values measured with clumped isotopes.

et al., 2004), and by radiogenic ε_{Nd} and unradiogenic $^{87}Sr/^{86}Sr$ values of sediments from the Umbria-March region (Kocsis et al., 2008).

Alternatively, it has been shown that large riverine inputs can also result in a deviation of the Sr isotope composition of neritic seawater from that of the global ocean (Bryant et al., 1995; El Meknassi et al., 2018). At Carry-le Rouet, the Miocene deposits unconformably rest on marine carbonates from the Lower Cretaceous (Barremian to Lower Aptian), that are characterized by low $^{87}Sr/^{86}Sr$ values (typically within the 0.7073 to 0.70745 range; McArthur and Howarth, 2004). Enhanced freshwater input should then result in a decrease of local seawater $^{87}Sr/^{86}Sr$, if large enough to impact the local Sr budget. Bryant et al. (1995) has shown that a measurable effect occurs at salinities below 12‰. Salinities calculated from our coupled $\delta^{18}O$-Δ_{47} approach lay however in the 30 to 34‰ range for this interval at Carry-le-Rouet, and the impact of freshwater inputs on the local seawater Sr isotope composition should then have remained limited. Yet recent studies reported that deviation from the global ocean $^{87}Sr/^{86}Sr$ value can occur at higher salinities, above 30‰ (Huang et al., 2011), especially in environments affected by submarine groundwater discharges that can have elevated Sr concentrations when deriving from carbonate-rock aquifer systems (Trezzi et al., 2017; El Meknassi et al., 2018). Thus enhanced riverine inputs may also have contributed to lower the $^{87}Sr/^{86}Sr$ value of the local seawater at Carry-le-Rouet.

Conversely, for the Late Burdigalian, the reconstructed salinities are much higher (p-value of 0.0014 using a *t*-test), in the 38 to 39‰ range (Table 2; Fig. 8D). This would correspond to a hypersaline environment with reduced runoff and high evaporation, in agreement with the higher temperatures inferred from our Δ_{47} analyzes in the Late Burdigalian compared to the Aquitanian. Such high salinities are consistent with the disappearance of stenohalin organisms and the restricted environmental conditions recorded at the Tamaris section. High evaporation should not affect $^{87}Sr/^{86}Sr$ values of seawater, which is coherent with the $^{87}Sr/^{86}Sr$ values recorded by our bivalves, mostly within the expected range of signature for the open ocean at that time.

The calculated salinities for the Langhian stage lay between 30 and 32‰ (Table 2; Fig. 8D), significantly lower than those calculated for the Burdigalian (p-value of 0.00002, using a *t*-test). Combined with the quite cool temperatures deduced from Δ_{47} for this period, this suggests again a marine environment subjected to freshwater inputs. A cooler and slightly brackish environment during the MMCO at Castillon-Du-Gard would agree with the proliferation of bryozoans and associated algae in these levels. Similar facies association is described in middle Miocene marine sediments from Austria and considered as deposited in a temperate environment with low salinity (Friebe, 1994). Modern bryozoan ecological reconstructions, occupy a wide variety of environments and can tolerate salinities ranging from 32 to 37‰ (Ryland, 1970; Smith, 1995) and temperatures from 10 to 30 °C (Domack, 1988), that are within the temperature and salinity ranges inferred from our coupled Δ_{47} - $\delta^{18}O$ approach at Castillon-Du-Gard.

The Sr isotope composition of Langhian bivalves from the Castillon-du-Gard section fall within the Sr isotope reference curve for the open ocean at that time (Fig. 8E), although our coupled $\delta^{18}O$-Δ_{47} approach points to salinities comparable to that obtained for the Aquitanian. Deviations toward more radiogenic values at that time were reported from mixed fossils from sites closer to the Alps, as exposure of older continental rocks contributes to imprint river waters with a radiogenic Sr isotope composition (Kocsis et al., 2008, 2009). Surface runoff issued from watersheds in Western Europe exhibits at present quite radiogenic Sr isotope signature (of 0,7093 on average; Peucker-Ehrenbrink and Fiske, 2019). The Castillon-du-Gard section, located north to the Carry-le-Rouet section within a narrow and incised valley, could have received a larger contribution from river waters draining the Alps watersheds, especially in the context of the tectonically-enhanced uplift of the Alps during the Miocene (Frisch et al., 2000; Reynaud et al., 2012). Rivers draining old continental material tend to yield much lower Sr concentrations than rivers or groundwaters draining carbonate lithologies. It is thus possible that the enhanced freshwater inputs during the MMCO, inferred from the salinities calculated from the $\delta^{18}O$ and Δ_{47} values, were not large enough at Castillon-du-Gard to significantly shift the local seawater $^{87}Sr/^{86}Sr$ ratio.

6. Conclusions

Our multi-proxy approach based on both $\delta^{18}O$ and Δ_{47} analyses of bivalves recovered from two outcrops in southern France during the Miocene highlight a warming (~3 °C) of the North-West Mediterranean coastal marine environments between the Aquitanian and the Late Burdigalian, accompanied by an increase in local salinity probably linked to more restricted conditions. Surprisingly, low $\delta^{18}O$ values recorded in the Langhian, supposedly during the MMCO, are associated with cooler seawater temperatures (between 13 and 18 °C) inferred from Δ_{47} analyzes. This apparent discrepancy can be reconciled if a modification occurred in the local hydrological cycle linked to the overall warmer conditions recorded at a global scale during this event, leading to enhanced discharges of freshwaters in the region during the MMCO. The existence of relatively cool and low salinity local waters would be consistent is with the development of an abundant bryozoan fauna observed at that time in the studied section. Local freshwater

discharges at the regional scale could also have been promoted by change in the pattern of the drainage system driven by local tectonic uplift and a narrowing of the corridor structure of the Rhodano-Provencal. The Sr isotope analyses performed on the bivalves from the two studied sections are compatible with the existence of freshwater inputs during the Aquitanian and the Langhian in this region. These inputs were however not large enough to result in large deviations of the local seawater $^{87}Sr/^{86}Sr$ composition from that of the global ocean, which is consistent with the reconstructed salinities, laying in the 30–34‰ range. Importantly, our results illustrate the risks inherent to paleotemperature reconstructions based solely on $\delta^{18}O$ records and highlight the pertinence of coupling several paleoenvironmental and paleoclimatic proxies, geochemical ($\delta^{18}O$ - Δ_{47}) or sedimentological, to reconstruct the variations of seawater temperature and salinity in shallow coastal environments. The combined $\delta^{18}O$ - Δ_{47} approach thus appears promising to study the local response to global climatic variations in environments that are subjected to salinity variations (lagoonal, mangrove or estuarine environments). Understanding how such environments react to climate change would help to better constrain the behavior of our climate system. Our work highlights the importance of a continuous effort in gathering new data from different regions of the world during MMCO, to capture the diversity of local responses to a global climatic change.

Supplementary data to this article can be found online at https://doi.org/10.1016/j.palaeo.2019.109582.

Declaration of competing interest

The authors declare that they have no known competing financial interests or personal relationships that could have appeared to influence the work reported in this paper.

Acknowledgements

We wish to thank T. COCQUEREZ (Biogeosciences Laboratory, University of Burgundy) and S. MOUNIC (Geosciences Environnement Toulouse Laboratory, University of Toulouse 3 Paul Sabatier) for the isotopic analyses. We wish also to thank F. MONNA and R. LAFFONT (Biogeosciences Laboratory, University of Burgundy) for help with statistical treatment of our data. This study was financed by ANR, France; AMOR project (16-CE31-0020) coordinated by Y. DONNADIEU.

References

Akgün, F., Kayseri, M.S., Akkiraz, M.S., 2007. Palaeoclimatic evolution and vegetational changes during the Late Oligocene–Miocene period in Western and Central Anatolia (Turkey). Palaeogeogr. Palaeoclimatol. Palaeoecol. 253 (1), 56–90. https://doi.org/10.1016/j.palaeo.2007.03.034.

Al-Aasm, I.S., Veizer, J., 1986. Diagenetic stabilization of aragonite and low-Mg calcite; I, Trace elements in rudists. J. Sediment. Res. 56 (1), 138–152. https://doi.org/10.1306/212F88A5-2B24-11D7-8648000102C1865D.

Anderson, T.F., Arthur, M.A., 1983. Stable isotopes of oxygen and carbon and their application to sedimentologic and paleoenvironmental problems. Unknown Journal.

Andreieff, P., Anglada, R., Carbonnel, G., Catzigras, F., Cavelier, C., Chateauneuf, J.J., Colomb, E., Jacob, C., Lai, J., l'Hommer, A., Lezaud, L., Lorenz, C., Mercier, H., Parfenoff, A., 1972. Contribution à l'étude de Carry-le-Rouet (Bouches-du-Rhône). Cinquième congrès du Néogène Méditerranéen. 3. Mémoire du BRGM, pp. 132.

Anglada, R., Gourinard, Y., Lesueur, J.L., Rubino, J.-L., 1988. Les séquences de dépôt du Burdigalien et du Langhien de Basse Provence (Littoral de la Nerthe et région des Etangs). In: Livret Guide d'Excursion Coll. « Paléobathymétrie, eustatisme et séquence de dépôts », Marseille, (juin 1988: 34p).

Arnaud, M., Barbaroux, L., Catzigras, F., Colomb, E., Monleau, C., 1988. Le Burdigalien et la Langhien de Provence occidentale (Bouches-du-Rhône): nouvelles données stratigraphiques et sédimentologiques. C. R. Acad. Sci. 307 (II), 779–784.

Beccaluva, L., Coltorti, M., Giunta, G., Siena, F., 2004. Tethyan vs. Cordilleran ophiolites: a reappraisal of distinctive tectono-magmatic features of supra-subduction complexes in relation to the subduction mode. Tectonophysics 393 (1–4), 163–174. https://doi.org/10.1016/j.tecto.2004.07.034.

Beddow, H.M., Liebrand, D., Sluijs, A., Wade, B.S., Lourens, L.J., 2016. Global change across the Oligocene-Miocene transition: high-resolution stable isotope records from IODP Site U1334 (equatorial Pacific Ocean). Paleoceanography 31 (1), 81–97. https://doi.org/10.1002/2015PA002820.

Bernasconi, S.M., Müller, I.A., Bergmann, K.D., Breitenbach, S.F., Fernandez, A., Hodell, D.A., Jaggi, M., Nele-Meckler, A., Millan, I., Ziegler, M., 2018. Reducing uncertainties in carbonate clumped isotope analysis through consistent carbonate-based standardization. Geochem. Geophys. Geosyst. 19 (9), 2895–2914. https://doi.org/10.1029/2017GC007385.

Bialik, O.M., Frank, M., Betzler, C., Zammit, R., Waldmann, N.D., 2019. Two-step closure of the Miocene Indian Ocean Gateway to the Mediterranean. Sci. Rep. 9 (1), 8842. https://doi.org/10.1038/s41598-019-45308-7.

Billups, K., Schrag, D.P., 2002. Paleotemperatures and ice volume of the past 27 Myr revisited with paired Mg/Ca and $^{18}O/^{16}O$ measurements on benthic foraminifera. Paleoceanography 17 (1). https://doi.org/10.1029/2000PA000567. (3–1).

Böhme, M., Bruch, A.A., Selmeier, A., 2007. The reconstruction of Early and Middle Miocene climate and vegetation in Southern Germany as determined from the fossil wood flora. Palaeogeogr. Palaeoclimatol. Palaeoecol. 253 (1), 91–114. https://doi.org/10.1016/j.palaeo.2007.03.035.

Borgovini, R., 2003. Stratigraphie et facies de la base du cycle Néogène de Basse Provence (littoral de la Nerthe : Carry-Le-Rouet, Sausset-Les-Pins). In: Rapport Total, Exploration and Production, DGEP/GSR/TG/THEM N°03–006, pp. 134.

Bosellini, F.R., Perrin, C., 2008. Estimating Mediterranean Oligocene–Miocene Sea-surface temperatures: an approach based on coral taxonomic richness. Palaeogeogr. Palaeoclimatol. Palaeoecol. 258 (1–2), 71–88. https://doi.org/10.1016/j.palaeo.2007.10.028.

Bougeault, C., Pellenard, P., Deconinck, J.F., Hesselbo, S.P., Dommergues, J.L., Bruneau, L., Cocquerez, T., Laffont, R., Huret, A., Thibault, N., 2017. Climatic and palaeoceanographic changes during the Pliensbachian (early Jurassic) inferred from clay mineralogy and stable isotope (CO) geochemistry (NW Europe). Glob. Planet. Chang. 149, 139–152. https://doi.org/10.1016/j.gloplacha.2017.01.005.

Bougeois, L., De Rafélis, M., Reichart, G.J., De Nooijer, L.J., Nicollin, F., Dupont-Nivet, G., 2014. A high resolution study of trace elements and stable isotopes in oyster shells to estimate Central Asian Middle Eocene seasonality. Chem. Geol. 363, 200–212. https://doi.org/10.1016/j.chemgeo.2013.10.037.

Bougeois, L., De Rafélis, M., Reichart, G.J., de Nooijer, L.J., Dupont-Nivet, G., 2016. Mg/Ca in fossil oyster shells as palaeotemperature proxy, an example from the Palaeogene of Central Asia. Palaeogeogr. Palaeoclimatol. Palaeoecol. 441, 611–626. https://doi.org/10.1016/j.palaeo.2015.09.052.

Brand, U., Veizer, J., 1981. Chemical diagenesis of a multicomponent carbonate system; 2, Stable isotopes. J. Sediment. Res. 51 (3), 987–997. https://doi.org/10.1306/212F7DF6-2B24-11D7-8648000102C1865D.

Brand, W.A., Assonov, S.S., Coplen, T.B., 2010. Correction for the ^{17}O interference in $\delta(^{13}C)$ measurements when analyzing CO_2 with stable isotope mass spectrometry (IUPAC Technical Report). Pure Appl. Chem. 82 (8), 1719–1733. https://doi.org/10.1351/PAC-REP-09-01-05.

Brown, J.R., Hartwick, E.B., 1988. Influences of temperature, salinity and available food upon suspended culture of the Pacific oyster, Crassostrea gigas: I. Absolute and allometric growth. Aquaculture 70 (3), 231–251. https://doi.org/10.1016/0044-8486(88)90099-3.

Bruch, A.A., Utescher, T., Olivares, C.A., Dolakova, N., Ivanov, D., Mosbrugger, V., 2004. Middle and Late Miocene Spatial Temperature Patterns and Gradients in Europe-Preliminary Results Based on Palaeobotanical Climate Reconstructions. Courier-Forschungsinstitut Senckenberg, pp. 15–28.

Bruch, A.A., Uhl, D., Mosbrugger, V., 2007. Miocene climate in Europe—patterns and evolution: a first synthesis of NECLIME. Palaeogeogr. Palaeoclimatol. Palaeoecol. 253 (1–2), 1–7. https://doi.org/10.1016/j.palaeo.2007.03.030.

Bruch, A.A., Utescher, T., Mosbrugger, V., 2011. Precipitation patterns in the Miocene of Central Europe and the development of continentality. Palaeogeogr. Palaeoclimatol. Palaeoecol. 304 (3–4), 202–211. https://doi.org/10.1016/j.palaeo.2010.10.002.

Bryant, J.D., Jones, D.S., Mueller, P.A., 1995. Influence of freshwater flux on 87 Sr/86 Sr chronostratigraphy in marginal marine environments and dating of vertebrate and invertebrate faunas. J. Paleontol. 69 (1), 1–6. https://doi.org/10.1017/S002233600002686X.

Choquette, P.W., James, N.P., 1990. Limestones—the burial diagenetic environment. In: Diagenesis: Geoscience Canada. Reprint Series 4. pp. 75–111.

Clark Jr., R.C., Finley, J.S., Gibson, G.G., 1974. Acute effects of outboard motor effluent on two marine shellfish. Environ. Sci. Technol. 8 (12), 1009–1014.

Cornacchia, I., Agostini, S., Brandano, M., 2018. Miocene oceanographic evolution based on the Sr and Nd isotope record of the central Mediterranean. Paleoceanography and Paleoclimatology 33 (1), 31–47. https://doi.org/10.1002/2017PA003198.

Cramwinckel, M.J., Huber, M., Kocken, I.J., Agnini, C., Bijl, P.K., Bohaty, S.M., Frieling, J., Goldner, A., Hilgen, F.J., Kip, E.L., Peterse, F., Van Der Ploeg, R., Röhl, U., Schouten, S., Sluijs, A., 2018. Synchronous tropical and polar temperature evolution in the Eocene. Nature 559 (7714), 382. https://doi.org/10.1038/s41586-018-0272-2.

Daëron, M., Blamart, D., Peral, M., Affek, H.P., 2016. Absolute isotopic abundance ratios and the accuracy of Δ_{47} measurements. Chem. Geol. 442, 83–96. https://doi.org/10.1016/j.chemgeo.2016.08.014.

Das Sharma, S., Patil, D.J., Gopalan, K., 2002. Temperature dependence of oxygen isotope fractionation of CO_2 from magnesite-phosphoric acid reaction. Geochim. Cosmochim. Acta 66 (4), 589–593. https://doi.org/10.1016/S0016-7037(01)00833-X.

de Winter, N.J.D., Vellekoop, J., Vorsselmans, R., Golreihan, A., Soete, J., Petersen, S.V., Meyer, K.W., Casadio, S., Speijer, R.P., Claeys, P., 2018. An assessment of latest cretaceous Pycnodonte vesicularis (Lamarck, 1806) shells as records for palaeoseasonality: a multi-proxy investigation. Clim. Past 14 (6), 725–749. https://doi.org/10.5194/cp-14-725-2018.

Demarcq, G., 1970. Étude stratigraphique du Miocène rhodanien. Mém. BRGM, n°61. (257 p).

Demory, F., Conesa, G., Oudet, J., Mansouri, H., Münch, P., Borgomano, J., Thouveny, N.,

Lamarche, J., Gisquet, F., Marié, L., 2011. Magnetostratigraphy and paleoenvironments in shallow-water carbonates: the Oligocene-Miocene sediments of the northern margin of the Liguro-Provençal basin (West Marseille, southeastern France). Bulletin de la Société géologique de France 182 (1), 37–55. https://doi.org/10.2113/gssgfbull.182.1.37.

Dera, G., Brigaud, B., Monna, F., Laffont, R., Pucéat, E., Deconinck, J.F., Pellenard, P., Joachimski, M.M., Durlet, C., 2011. Climatic ups and downs in a disturbed Jurassic world. Geology 39 (3), 215–218. https://doi.org/10.1130/G31579.1.

Diester-Haass, L., Billups, K., Gröcke, D.R., François, L., Lefebvre, V., Emeis, K.C., 2009. Mid-Miocene paleoproductivity in the Atlantic Ocean and implications for the global carbon cycle. Paleoceanography and Paleoclimatology 24 (1). https://doi.org/10.1029/2008PA001605.

Do Couto, D., Gorini, C., Jolivet, L., Lebret, N., Augier, R., Gumiaux, C., d'Acremont, E., Ammar, A., Jabour, H., Auxietre, J.L., 2016. Tectonic and stratigraphic evolution of the Western Alboran Sea Basin in the last 25 Myrs. Tectonophysics 677, 280–311. https://doi.org/10.1016/j.tecto.2016.03.020.

Domack, E.W., 1988. Biogenic facies in the Antarctic glacimarine environment: basis for a polar glacimarine summary. Palaeogeogr. Palaeoclimatol. Palaeoecol. 63 (4), 357–372. https://doi.org/10.1016/0031-0182(88)90105-8.

Eiler, J.M., Bonifacie, M., Daëron, M., 2009. 'Clumped isotope' thermometry for high-temperature problems. Geochim. Cosmochim. Acta 73 (13), A318–A347. https://doi.org/10.1016/j.gca.2009.05.004.

El Meknassi, S., Dera, G., Cardone, T., De Rafélis, M., Brahmi, C., Chavagnac, V., 2018. Sr isotope ratios of modern carbonate shells: good and bad news for chemostratigraphy. Geology 46 (11), 1003–1006. https://doi.org/10.1130/G45380.1.

Faccenna, C., Mattei, M., Funiciello, R., Jolivet, L., 1997. Styles of back-arc extension in the central Mediterranean. Terra Nova 9 (3), 126–130. https://doi.org/10.1046/j.1365-3121.1997.d01-12.x.

Ferrandini, M., BouDagher-Fadel, M.K., Ferrandini, J., Oudet, J., André, J.P., 2010. Nouvelles observations sur les Miogypsinidés du Miocène inférieur et moyen de Provence et de Corse (France) et de Sardaigne septentrionale (Italie). Annales de Paléontologie 96 (3), 67–94. https://doi.org/10.1016/j.annpal.2011.04.002.

Fondecave-Wallez, M.J., Magné, J., Gourinard, Y., Demarcq, G., 1986. Nouvelles grade-datations de sédiments burdigaliens des régions rhodaniennes. Géologie Méditerranéenne 12 (1), 59–63. https://doi.org/10.3406/geolm.1985.1339.

Foster, G.L., Lear, C.H., Rae, J.W., 2012. The evolution of pCO_2, ice volume and climate during the middle Miocene. Earth Planet. Sci. Lett. 341, 243–254. https://doi.org/10.1016/j.epsl.2012.06.007.

Friebe, J.G., 1994. Serpulid-bryozoan-foraminiferal biostromes controlled by temperate climate and reduced salinity: Middle Miocene of the Styrian Basin, Austria. Facies 30 (1), 51–62. https://doi.org/10.1007/BF02536889.

Frisch, W., Dunkl, I., Kuhlemann, J., 2000. Post-collisional orogen-parallel large-scale extension in the Eastern Alps. Tectonophysics 327 (3–4), 239–265. https://doi.org/10.1016/S0040-1951(00)00204-3.

Frizon de Lamotte, D., Saint Bezar, B., Bracène, R., Mercier, E., 2000. The two main steps of the Atlas building and geodynamics of the western Mediterranean. Tectonics 19 (4), 740–761. https://doi.org/10.1029/2000TC900003.

Galeotti, S., DeConto, R., Naish, T., Stocchi, P., Florindo, F., Pagani, M., Barrett, P., Bohaty, S.M., Lanci, L., Pollard, D., Sandroni, S., Talarico, F.M., Zachos, J.C., 2016. Antarctic Ice Sheet variability across the Eocene-Oligocene boundary climate transition. Science 352 (6281), 76–80. https://doi.org/10.1126/science.aab0669.

Gasson, E., DeConto, R.M., Pollard, D., Levy, R.H., 2016. Dynamic Antarctic ice sheet during the early to mid-Miocene. Proc. Natl. Acad. Sci. 113 (13), 3459–3464. https://doi.org/10.1073/pnas.1516130113.

Gattacceca, J., Deino, A., Rizzo, R., Jones, D.S., Henry, B., Beaudoin, B., Vadeboin, F., 2007. Miocene rotation of Sardinia: New paleomagnetic and geochronological constraints and geodynamic implications. Earth Planet. Sci. Lett. 258 (3–4), 359–377. https://doi.org/10.1016/j.epsl.2007.02.003.

Ghosh, P., Adkins, J., Affek, H., Balta, B., Guo, W., Schauble, E.A., Schrag, D., Eiler, J.M., 2006. ^{13}C–^{18}O bonds in carbonate minerals: a new kind of paleothermometer. Geochim. Cosmochim. Acta 70 (6), 1439–1456. https://doi.org/10.1016/j.gca.2005.11.014.

Goedert, J., Amiot, R., Arnaud-Godet, F., Cuny, G., Fourel, F., Hernandez, J.A., Pedreira-Segade, U., Lecuyer, C., 2017. Miocene (Burdigalian) seawater and air temperatures estimated from the geochemistry of fossil remains from the Aquitaine Basin, France. Palaeogeogr. Palaeoclimatol. Palaeoecol. 481, 14–28. https://doi.org/10.1016/j.palaeo.2017.04.024.

Goldner, A., Herold, N., Huber, M., 2014. The challenge of simulating the warmth of the mid-Miocene climatic optimun in CESM1. Clim. Past 10, 523–536. https://doi.org/10.5194/cp-10-523-2014.

Grossman, E.L., 2012. Applying oxygen isotope paleothermometry in deep time. The Paleontological Society Papers 18, 39–68. https://doi.org/10.1017/S1089332600002540.

Gueguen, E., Doglioni, C., Fernandez, M., 1998. On the post-25 Ma geodynamic evolution of the western Mediterranean. Tectonophysics 298 (1–3), 259–269. https://doi.org/10.1016/S0040-1951(98)00189-9.

Hamon, Y., Santerre, Y., Granjeon, D., Conesa, G., Borgomano, J., 2013. Early diagenesis in meteoric versus brackish environments: example of the Late Oligocene-Early Miocene, littoral, mixed sedimentary succession of Carry-Le-Rouet (southeastern France). Bulletin de la Société géologique de France 184 (6), 601–620. https://doi.org/10.2113/gssgfbull.184.6.601.

Hannig, J., Marron, J.S., 2006. Advanced distribution theory for SiZer. J. Am. Stat. Assoc. 101 (474), 484–499.

Harzhauser, M., Piller, W.E., Müllegger, S., Grunert, P., Micheels, A., 2011. Changing seasonality patterns in central Europe from Miocene climate optimum to Miocene climate transition deduced from the Crassostrea isotope archive. Glob. Planet. Chang. 76 (1–2), 77–84. https://doi.org/10.1016/j.gloplacha.2010.12.003.

Henkes, G.A., Passey, B.H., Wanamaker Jr., A.D., Grossman, E.L., Ambrose Jr., W.G., Carroll, M.L., 2013. Carbonate clumped isotope compositions of modern marine mollusk and brachiopod shells. Geochim. Cosmochim. Acta 106, 307–325. https://doi.org/10.1016/j.gca.2012.12.020.

Holbourn, A., Kuhnt, W., Schulz, M., Erlenkeuser, H., 2005. Impacts of orbital forcing and atmospheric carbon dioxide on Miocene ice-sheet expansion. Nature 438 (7067), 483. https://doi.org/10.1038/nature04123.

Holbourn, A., Kuhnt, W., Kochhann, K.G., Andersen, N., Sebastian Meier, K.J., 2015. Global perturbation of the carbon cycle at the onset of the Miocene Climatic Optimum. Geology 43 (2), 123–126. https://doi.org/10.1130/G36317.1.

Holmes, A., 1965. Principles of Physical Geology, 2nd edn. Thomas Nelson, London (1288 pp).

Huang, K.F., You, C.F., Chung, C.H., Lin, I.T., 2011. Nonhomogeneous seawater Sr isotopic composition in the coastal oceans: a novel tool for tracing water masses and submarine groundwater discharge. Geochem. Geophys. Geosyst. 12 (5). https://doi.org/10.1029/2010GC003372.

Huyghe, D., Mouthereau, F., Emmanuel, L., 2012. Oxygen isotopes of marine mollusc shells record Eocene elevation change in the Pyrenees. Earth Planet. Sci. Lett. 345, 131–141. https://doi.org/10.1016/j.epsl.2012.06.035.

Huyghe, D., Lartaud, F., Emmanuel, L., Merle, D., Renard, M., 2015. Palaeogene climate evolution in the Paris Basin from oxygen stable isotope ($\delta^{18}O$) compositions of marine molluscs. J. Geol. Soc. 172 (5), 576–587. https://doi.org/10.1144/jgs2015-016.

Huyghe, D., de Rafélis, M., Ropert, M., Mouchi, V., Emmanuel, L., Renard, M., Lartaud, F., 2019. New insights into oyster high-resolution hinge growth patterns. Mar. Biol. 166 (4), 48. https://doi.org/10.1007/s00227-019-3496-2.

Ingram, B.L., Sloan, D., 1992. Strontium isotopic composition of estuarine sediments as paleosalinity-paleoclimate indicator. Science 255 (5040), 68–72. https://doi.org/10.1126/science.255.5040.68.

Ivany, L.C., Patterson, W.P., Lohmann, K.C., 2000. Cooler winters as a possible cause of mass extinctions at the Eocene/Oligocene boundary. Nature 407 (6806), 887. https://doi.org/10.1038/35038044.

Jiménez-Moreno, G., Suc, J.P., 2007. Middle Miocene latitudinal climatic gradient in Western Europe: evidence from pollen records. Palaeogeogr. Palaeoclimatol. Palaeoecol. 253 (1–2), 208–225. https://doi.org/10.1016/j.palaeo.2007.03.040.

Jiménez-Moreno, G., Fauquette, S., Suc, J.P., 2010. Miocene to Pliocene vegetation reconstruction and climate estimates in the Iberian Peninsula from pollen data. Rev. Palaeobot. Palynol. 162 (3), 403–415. https://doi.org/10.1016/j.revpalbo.2009.08.001.

Jolivet, L., Augier, R., Robin, C., Suc, J.P., Rouchy, J.M., 2006. Lithospheric-scale geodynamic context of the Messinian salinity crisis. Sediment. Geol. 188, 9–33. https://doi.org/10.1016/j.sedgeo.2006.02.004.

Kirby, M.X., Soniat, T.M., Spero, H.J., 1998. Stable isotope sclerochronology of Pleistocene and recent oyster shells (Crassostrea virginica). Palaios 13 (6), 560–569. https://doi.org/10.2307/3515347.

Klein, R.T., Lohmann, K.C., Thayer, C.W., 1996. Sr/Ca and $^{13}C/^{12}C$ ratios in skeletal calcite of Mytilus trossulus: covariation with metabolic rate, salinity, and carbon isotopic composition of seawater. Geochim. Cosmochim. Acta 60, 4207–4221. https://doi.org/10.1016/S0016-7037(96)00232-3.

Kocsis, L., Vennemann, T.W., Fontignie, D., Baumgartner, C., Montanari, A., 2008. Oceanographic and climatic evolution of the Miocene Mediterranean deduced from Nd, Sr, C, and O isotope compositions of marine fossils and sediments. Paleoceanography 23, PA4211. https://doi.org/10.1029/2007PA001540.

Kocsis, L., Vennemann, T.W., Hegner, E., Fontignie, D., Tütken, T., 2009. Constraints on Miocene oceanography and climate in the Western and Central Paratethys: O-, Sr-, and Nd-isotope compositions of marine fish and mammal remains. Palaeogeogr. Palaeoclimatol. Palaeoecol. 271 (1–2), 117–129. https://doi.org/10.1016/j.palaeo.2008.10.003.

Langlet, D., Alunno-Bruscia, M., Rafélis, M., Renard, M., Roux, M., Schein, E., Buestel, D., 2006. Experimental and natural cathodoluminescence in the shell of Crassostrea gigas from Thau lagoon (France): ecological and environmental implications. Mar. Ecol. Prog. Ser. 317, 143–156. https://doi.org/10.3354/meps317143.

Lartaud, F., Langlet, D., De Rafelis, M., Emmanuel, L., Renard, M., 2006. Mise en évidence de rythmicité saisonnière dans la coquille des huîtres fossiles Crassostrea aginensis Tournouer, 1914 (Aquitanien) et Ostrea bellovacina Lamarck, 1806 (Thanétien). Approche par cathodoluminescence et par sclérochronologie. Geobios 39 (6), 845–852. https://doi.org/10.1016/j.geobios.2005.11.001.

Lartaud, F., De Rafélis, M., Ropert, M., Emmanuel, L., Geairon, P., Renard, M., 2010. Mn labelling of living oysters: artificial and natural cathodoluminescence analyses as a tool for age and growth rate determination of C. gigas (Thunberg, 1793) shells. Aquaculture 300 (1–4), 206–217. https://doi.org/10.1007/s10347-009-0196-2.

Lear, C.H., Bailey, T.R., Pearson, P.N., Coxall, H.K., Rosenthal, Y., 2008. Cooling and ice growth across the Eocene-Oligocene transition. Geology 36 (3), 251–254. https://doi.org/10.1130/G24584A.1.

Lear, C.H., Coxall, H.K., Foster, G.L., Lunt, D.J., Mawbey, E.M., Rosenthal, Y., Sosdian, S.M., Thomas, E., Wilson, P.A., 2015. Neogene ice volume and ocean temperatures: Insights from infaunal foraminiferal Mg/Ca paleothermometry. Paleoceanography 30 (11), 1437–1454. https://doi.org/10.1002/2015PA002833.

Lecuyer, C., Grandjean, P., Paris, F., Robardet, M., Robineau, D., 1996. Deciphering "temperature" and "salinity" from biogenic phosphates: the $\delta^{18}O$ of coexisting fishes and mammals of the Middle Miocene Sea of western France. Palaeogeogr. Palaeoclimatol. Palaeoecol. 126 (1–2), 61–74. https://doi.org/10.1016/S0031-0182(96)00070-3.

Levitus, S., Boyer, T.P., 1994. World Ocean Atlas 1994. Volume 4. Temperature (No. PB-95-270112/XAB; NESDIS-4). National Environmental Satellite, Data, and Information

Service, Washington, DC (United States).
Liu, Z., Pagani, M., Zinniker, D., DeConto, R., Huber, M., Brinkhuis, H., Shah, S.R., Leckie, M., Pearson, A., 2009. Global cooling during the Eocene-Oligocene climate transition. Science 323 (5918), 1187–1190. https://doi.org/10.1126/science.1166368.
Marron, J.S., Chaudhuri, P., 1998. When is a feature really there: the SiZer approach. In: Automatic Target Recognition VIII. 3371. International Society for Optics and Photonics, pp. 306–313. https://doi.org/10.1117/12.323850.
Maurel-ferrandini, M., 1976. Reconstitution paléogéographique du Burdigalien du littoral de la chaîne de la Nerthe et de la région des étangs (Bouches-du-Rhône, France). PhD Thesis. University of Provence, Marseille (87 p).
Mawbey, E.M., Lear, C.H., 2013. Carbon cycle feedbacks during the Oligocene-Miocene transient glaciation. Geology 41 (9), 963–966. https://doi.org/10.1130/G34422.1.
McArthur, J., Howarth, R.J., 2004. Strontium isotope stratigraphy. In: Gradstein, F., Ogg, J., Smith, A. (Eds.), A Geologic Time Scale. Cambridge University Press, Cambridge, pp. 96–105.
Meckler, A.N., Ziegler, M., Millán, M.I., Breitenbach, S.F., Bernasconi, S.M., 2014. Long-term performance of the Kiel carbonate device with a new correction scheme for clumped isotope measurements. Rapid Commun. Mass Spectrom. 28 (15), 1705–1715. https://doi.org/10.1002/rcm.6949.
Miall, A.D., 1986. Eustatic sea level changes interpreted from seismic stratigraphy: a critique of methodology with particular reference to the North Sea Jurassic record. AAPG Bull. 70, 131–137.
Miller, K.G., Wright, J.D., Fairbanks, R.G., 1991. Unlocking the ice house: Oligocene-Miocene oxygen isotopes, eustasy, and margin erosion. Journal of Geophysical Research: Solid Earth 96 (B4), 6829–6848. https://doi.org/10.1029/90JB02015.
Mitchell, I.M., Crawford, C.M., Rushton, M.J., 2000. Flat oyster (Ostrea angasi) growth and survival rates at Georges Bay, Tasmania (Australia). Aquaculture 191 (4), 309–321. https://doi.org/10.1016/S0044-8486(00)00441-5.
Montanari, A., Carey, S., Coccioni, R., Deino, A., 1994. Early Miocene tephra in the Apennine pelagic sequence: an inferred Sardinian provenance and implications for western Mediterranean tectonics. Tectonics 13 (5), 1120–1134. https://doi.org/10.1029/94TC00295.
Mosbrugger, V., Utescher, T., Dilcher, D.L., 2005. Cenozoic continental climatic evolution of Central Europe. PNAS 102 (42), 14964–14969. https://doi.org/10.1073/pnas.0505267102.
Mouchi, V., Briard, J., Gaillot, S., Argant, T., Forest, V., Emmanuel, L., 2018. Reconstructing environments of collection sites from archaeological bivalve shells: case study from oysters (Lyon, France). J. Archaeol. Sci. Rep. 21, 1225–1235. https://doi.org/10.1016/j.jasrep.2017.10.025.
Nalin, R., Ghinassi, M., Basso, D., 2010. Onset of temperate carbonate sedimentation during transgression in a low-energy siliciclastic embayment (Pliocene of the Val d'Orcia Basin, Tuscany, Italy). Facies 56 (3), 353–368. https://doi.org/10.1007/s10347-010-0211-7.
Nayar, K.G., Panchanathan, D., McKinley, G.H., Lienhard, J.H., 2014. Surface tension of seawater. J. Phys. Chem. Ref. Data 43 (4), 043103. https://doi.org/10.1063/1.4899037.
Nemec, W., Steel, R.J., 1988. What is a fan delta and how do we recognize it. In: Fan Deltas: Sedimentology and Tectonic Settings, pp. 3–13.
Nury, D., 1990. L'Oligocène de Provence méridionale: stratigraphie, dynamique sédimentaire, reconstitutions paléogéographiques. PhD Thesis. University of Provence, Marseille (411 p).
Oertli, H.J., 1964. The Venice system for the classification of marine waters according to salinity. Publicazioni della Stazione Zoologica di Napoli 33 (Supplement), 611.
Ogg, J.G., Ogg, G., Gradstein, F.M., 2016. A Concise Geologic Time Scale: 2016. Elsevierhttps://doi.org/10.1016/C2009-0-64442-1.
Ohno, T., Hirata, T., 2007. Simultaneous determination of mass-dependent isotopic fractionation and radiogenic isotope variation of strontium in geochemical samples by multiple collector-ICP-mass spectrometry. Anal. Sci. 23 (11), 1275–1280. https://doi.org/10.2116/analsci.23.1275.
Oudet, J., Münch, P., Borgomano, J., Quillevere, F., Melinte-Dobrinescu, M.C., Demory, F., Viseur, S., Cornee, J.J., 2010. Land and sea study of the northeastern golfe du Lion rifted margin: the Oligocene–Miocene of southern Provence (Nerthe area, SE France). Bulletin de la Société géologique de France 181 (6), 591–607. https://doi.org/10.2113/gssgfbull.181.6.591.
Pagani, M., Arthur, M.A., Freeman, K.H., 1999. Miocene evolution of atmospheric carbon dioxide. Paleoceanography 14 (3), 273–292. https://doi.org/10.1029/1999PA900006.
Palmer, M.R., Elderfield, H., 1985. Sr isotope composition of sea water over the past 75 Myr. Nature 314 (6011), 526. https://doi.org/10.1038/314526a0.
Passey, B.H., Henkes, G.A., 2012. Carbonate clumped isotope bond reordering and geospeedometry. Earth Planet. Sci. Lett. 351, 223–236. https://doi.org/10.1016/j.epsl.2012.07.021.
Paulet, Y.M., Lorrain, A., Richard, J., Pouvreau, S., 2006. Experimental shift in diet $\delta^{13}C$: a potential tool for ecophysiological studies in marine bivalves. Org. Geochem. 37 (10), 1359–1370. https://doi.org/10.1016/j.orggeochem.2006.01.008.
Peral, M., Daëron, M., Blamart, D., Bassinot, F., Dewilde, F., Smialkowski, N., Isguder, G., Bonnin, J., Jorissen, F., Kissel, C., Michel, E., Vaszquez Riveiros, N., Waelbroeck, C., 2018. Updated calibration of the clumped isotope thermometer in planktonic and benthic foraminifera. Geochim. Cosmochim. Acta 239, 1–16. https://doi.org/10.1016/j.gca.2018.07.016.
Petersen, S.V., Defliese, W.F., Saenger, C., Daëron, M., Huntington, K.W., John, C.M., Kelson, J.R., Bernasconi, S.M., Colman, A.S., Klug, T., Olack, G.A., Schauer, A.J., Bajnai, D., Bonifacie, M., Breitenbach, S.F.M., Fiebig, J., Fernandez, A.B., Henkes, G.A., Hodell, D., Katz, A., Kele, S., Lohmann, K.C., Passey, B.H., Peral, M.Y., Petrizzo, D.A., Rosenheim, B.E., Tripati, A., Venturelli, R., Young, E.D., Winkelstern, I.Z., 2019. Effects of improved ^{17}O correction on inter-laboratory agreement in clumped isotope calibrations, estimates of mineral-specific offsets, and temperature dependence of acid digestion fractionation. Geochem. Geophys. Geosyst. 20 (7), 3495–3519. https://doi.org/10.1029/2018GC008127.
Peucker-Ehrenbrink, B., Fiske, G.J., 2019. A continental perspective of the seawater $^{87}Sr/^{86}Sr$ record: a review. Chem. Geol. 510, 140–165. https://doi.org/10.1016/j.chemgeo.2019.01.017.
Pierre, C., 1999. The oxygen and carbon isotope distribution in the Mediterranean water masses. Mar. Geol. 153, 41–55. https://doi.org/10.1016/S0025-3227(98)00090-5.
Pound, M.J., Haywood, A.M., Salzmann, U., Riding, J.B., 2012. Global vegetation dynamics and latitudinal temperature gradients during the Mid to Late Miocene (15.97–5.33 Ma). Earth Sci. Rev. 112 (1–2), 1–22. https://doi.org/10.1016/j.earscirev.2012.02.005.
R Core Team, 2017. R: A Language and Environment for Statistical Computing. R Foundation for Statistical Computing, Vienna, Austria. https://www.R-project.org/.
Railsback, L.B., Anderson, T.F., 1989. Paleoceanographic modeling of temperature-salinity profiles from stable isotopic data. Paleoceanography 4, 801–814. https://doi.org/10.1029/PA004i005p00585.
Randazzo, A.F., Muller, P., Lelkes, G., Juhasz, E., Hamor, T., 1999. Cool-water limestones of the Pannonian basinal system, Middle Miocene, Hungary. J. Sediment. Res. 69 (1), 283–293. https://doi.org/10.2110/jsr.69.283.
Rehault, J.P., Boillot, G., Mauffret, A., 1984. The western Mediterranean basin geological evolution. Mar. Geol. 55 (3–4), 447–477. https://doi.org/10.1016/0025-3227(84)90081-1.
Reuter, M., Piller, W.E., Brandano, M., Harzhauser, M., 2013. Correlating Mediterranean shallow water deposits with global Oligocene–Miocene stratigraphy and oceanic events. Glob. Planet. Chang. 111, 226–236. https://doi.org/10.1016/j.gloplacha.2013.09.018.
Reynaud, J.Y., Dalrymple, R.W., Vennin, E., Parize, O., Besson, D., Rubino, J.L., 2006. Topographic controls on production and deposition of tidal cool-water carbonates, Uzes Basin, SE France. J. Sediment. Res. 76 (1), 117–130. https://doi.org/10.2110/jsr.2006.07.
Reynaud, J.Y., Vennin, E., Parize, O., Rubino, J.L., Bourdillon, C., 2012. Incised valleys and tidal seaways: the example of the Miocene Uzès-Castillon basin, SE France. Bulletin de la Société Géologique de France 183 (5), 471–486. https://doi.org/10.2113/gssgfbull.183.5.471.
Riegl, B., Piller, W.E., 2000. Biostromal coral facies—a Miocene example from the Leitha Limestone (Austria) and its actualistic interpretation. Palaios 15 (5), 399–413. https://doi.org/10.1669/0883-1351(2000)015<0399:BCFAME>2.0.CO;2.
Ryland, J.S., 1970. Bryozoans. Hutchinson Univ. Library, London, pp. 175.
Schauble, E.A., Ghosh, P., Eiler, J.M., 2006. Preferential formation of ^{13}C–^{18}O bonds in carbonate minerals, estimated using first-principles lattice dynamics. Geochim. Cosmochim. Acta 70 (10), 2510–2529. https://doi.org/10.1016/j.gca.2006.02.011.
Schettino, A., Turco, E., 2011. Tectonic history of the western Tethys since the Late Triassic. Bulletin 123 (1–2), 89–105. https://doi.org/10.1130/B30064.1.
Schöne, B.R., 2008. The curse of physiology—challenges and opportunities in the interpretation of geochemical data from mollusk shells. Geo-Mar. Lett. 28 (5–6), 269–285. https://doi.org/10.1007/s00367-008-0114-6.
Schöne, B.R., Giere, O., 2005. Growth increments and stable isotope variation in shells of the deep-sea hydrothermal vent bivalve mollusk Bathymodiolus brevior from the North Fiji Basin, Pacific Ocean. Deep-Sea Res. I Oceanogr. Res. Pap. 52 (10), 1896–1910. https://doi.org/10.1016/j.dsr.2005.06.003.
Seibel, M.J., James, N.P., 2017. Diagenesis of Miocene, incised valley-filling limestones; Provence, Southern France. Sediment. Geol. 347, 21–35. https://doi.org/10.1016/j.sedgeo.2016.09.006.
Shevenell, A.E., Kennett, J.P., Lea, D.W., 2004. Middle Miocene southern ocean cooling and Antarctic cryosphere expansion. Science 305 (5691), 1766–1770. https://doi.org/10.1126/science.1100061.
Shevenell, A.E., Kennett, J.P., Lea, D.W., 2008. Middle Miocene ice sheet dynamics, deep-sea temperatures, and carbon cycling: a Southern Ocean perspective. Geochem. Geophys. Geosyst. 9 (2). https://doi.org/10.1029/2007GC001736.
Smith, A.M., 1995. Palaeoenvironmental interpretation using bryozoans: a review. Geol. Soc. Lond., Spec. Publ. 83 (1), 231–243. https://doi.org/10.1144/GSL.SP.1995.083.01.11.
Sonderegger, D., Sonderegger, M.D., 2018. Package 'SiZer'.
Stenzel, H.B., 1971. Oysters. Treatise on invertebrate paleontology, Part N. Bivalvia 3, N953–N1224.
Steuber, T., Rauch, M., Masse, J.P., Graaf, J., Malkoč, M., 2005. Low-latitude seasonality of cretaceous temperatures in warm and cold episodes. Nature 437 (7063), 1341. https://doi.org/10.1038/nature04096.
Stolper, D.A., Eiler, J.M., 2015. The kinetics of solid-state isotope-exchange reactions for clumped isotopes: a study of inorganic calcites and apatites from natural and experimental samples. Am. J. Sci. 315 (5), 363–411. https://doi.org/10.2475/05.2015.01.
Super, J.R., Thomas, E., Pagani, M., Huber, M., O'Brien, C., Hull, P.M., 2018. North Atlantic temperature and pCO_2 coupling in the early-middle Miocene. Geology 46 (6), 519–522. https://doi.org/10.1130/G40228.1.
Surge, D., Lohmann, K.C., Dettman, D.L., 2001. Controls on isotopic chemistry of the American oyster, Crassostrea virginica: implications for growth patterns. Palaeogeogr. Palaeoclimatol. Palaeoecol. 172 (3–4), 283–296. https://doi.org/10.1016/S0031-0182(01)00303-0.
Taylor, P.D., James, N.P., 2013. Secular changes in colony-forms and bryozoan carbonate sediments through geological history. Sedimentology 60 (5), 1184–1212. https://doi.org/10.1111/sed.12032.
Tempier, C., 1987. Modèle nouveau de mise en place des structures provencales. Bulletin Société Géologique France 8 (3), 533–540. https://doi.org/10.2113/gssgfbull.III.3.533.

Tremblin, M., Hermoso, M., Minoletti, F., 2016. Equatorial heat accumulation as a long-term trigger of permanent Antarctic ice sheets during the Cenozoic. Proc. Natl. Acad. Sci. 113 (42), 11782–11787. https://doi.org/10.1073/pnas.1608100113.

Trezzi, G., Garcia-Orellana, J., Rodellas, V., Masqué, P., Garcia-Solsona, E., Andersson, P.S., 2017. Assessing the role of submarine groundwater discharge as a source of Sr to the Mediterranean Sea. Geochim. Cosmochim. Acta 200, 42–54. https://doi.org/10.1016/j.gca.2016.12.005.

Ullmann, C.V., Wiechert, U., Korte, C., 2010. Oxygen isotope fluctuations in a modern North Sea oyster (Crassostrea gigas) compared with annual variations in seawater temperature: implications for palaeoclimate studies. Chem. Geol. 277 (1–2), 160–166. https://doi.org/10.1016/j.chemgeo.2010.07.019.

Ullmann, C.V., Campbell, H.J., Frei, R., Hesselbo, S.P., von Strandmann, P.A.P., Korte, C., 2013. Partial diagenetic overprint of Late Jurassic belemnites from New Zealand: implications for the preservation potential of δ7Li values in calcite fossils. Geochim. Cosmochim. Acta 120, 80–96. https://doi.org/10.1016/j.gca.2013.06.029.

van Hinsbergen, D.J., Torsvik, T.H., Schmid, S.M., Maţenco, L.C., Maffione, M., Vissers, R.L., Gürer, D., Spakman, W., 2019. Orogenic architecture of the Mediterranean region and kinematic reconstruction of its tectonic evolution since the Triassic. Gondwana Res. https://doi.org/10.1016/j.gr.2019.07.009.

Veizer, J., Ala, D., Azmy, K., Bruckschen, P., Buhl, D., Bruhn, F., Carden, G., Diener, A., Godderis, Y., Jasper, T., Korte, C., Pawellek, F., Podlaha, O., Strauss, H., 1999. 87Sr/86Sr, δ13C and δ18O evolution of Phanerozoic seawater. Chem. Geol. 161 (1–3), 59–88. https://doi.org/10.1016/S0009-2541(99)00081-9.

Weckström, J., Korhola, A., Erästö, P., Holmström, L., 2006. Temperature patterns over the past eight centuries in Northern Fennoscandia inferred from sedimentary diatoms. Quat. Res. 66 (1), 78–86. https://doi.org/10.1016/j.yqres.2006.01.005.

Widerlund, A., Andersson, P.S., 2006. Strontium isotopic composition of modern and Holocene mollusc shells as a palaeosalinity indicator for the Baltic Sea. Chem. Geol. 232 (1–2), 54–66. https://doi.org/10.1016/j.chemgeo.2006.02.010.

Yeghicheyan, D., Bossy, C., Le Coz, M.B., Douchet, C., Granier, G., Heimburger, A., Lacan, F., Lanzanova, A., Rousseau, T., Seidel, J., Tharaud, M., Candaudap, F., Chmeleff, J., Cloquet, C., Delpoux, S., Labatut, M., Losno, R., Pradoux, C., Sivry, Y., Sonke, J.E., 2013. A compilation of silicon, rare earth element and twenty-one other trace element concentrations in the natural river water reference material SLRS-5 (NRC-CNRC). Geostand. Geoanal. Res. 37 (4), 449–467. https://doi.org/10.1111/j.1751-908X.2013.00232.x.

Zachos, J.C., Quinn, T.M., Salamy, K.A., 1996. High-resolution (104 years) deep-sea foraminiferal stable isotope records of the Eocene-Oligocene climate transition. Paleoceanography 11 (3), 251–266. https://doi.org/10.1029/96PA00571.

Zachos, J., Pagani, M., Sloan, L., Thomas, E., Billups, K., 2001. Trends, rhythms, and aberrations in global climate 65 Ma to present. Science 292 (5517), 686–693. https://doi.org/10.1126/science.1059412.

Zachos, J.C., Dickens, G.R., Zeebe, R.E., 2008. An early Cenozoic perspective on greenhouse warming and carbon-cycle dynamics. Nature 451 (7176), 279. https://doi.org/10.1038/nature06588.

Zaky, A.H., Brand, U., Buhl, D., Blamey, N., Bitner, M.A., Logan, A., Gaspard, D., Popov, A., 2018. Strontium isotope geochemistry of modern and ancient archives: tracer of secular change in ocean chemistry. Can. J. Earth Sci. 56 (3), 245–264. https://doi.org/10.1139/cjes-2018-0085.